UNIVERSITY OF TARTU
INSTITUTE OF ECOLOGY AND EARTH SCIENCES
DEPARTMENT OF GEOLOGY

Kärt Üpraus

Chert-dolostone sequences in Zaonega Formation, Karelia: implication to the chert origin

MSc thesis

Supervisor: Kalle Kirsimäe

TARTU 2014

Table of Contents

Introduction 3
Geological setting 5
Materials and methods 7
Charge contrast imaging 12
Results 14
Petrography 14
Chert 14
Dolostone 17
Contact zones 21
Microdubiofossils 26
Mineralogy and chemistry 28
Isotope composition 33
Discussion 39
Conclusions 42
Acknowledgments 43
References 44
Zaonega kihistu dolokivide ränistumine 49

Introduction

Paleoproterozoic Zaonega Formation is a unique volcano-sedimentary succession in the Onega Basin, Karelia, NW Russia. The Zaonega succession is composed of mixed in places organic rich siliciclastic-carbonate sediments intersected by numerous syndepositional mafic lavas and sills, indicating a rift basin depositional environment on an active continental margin (Črne et al., 2012a, b; Melezhik et al., 2012). The complexity and uniqueness of the Zaonega Formation has been of interest for a long time (Melezhik et al., 2012). Foremost, the voluminous syndepositional mafic volcanism was responsible for triggering one of the earliest known petroleum generations in organic-rich mudstones in proximity of the igneous bodies (Črne et al., 2012a, b; Lepland et al., 2014; Strauss et al., 2012). Sediments passing through the oil window initiated hydrocarbon generation and migration resulting in asphalt spilling (mud volcanos) and petroleum seepage onto the sea floor, coeval and/or shortly post-dating the sedimentation (Melezhik et al., 2004). Sedimentary rocks pervasively impregnated with migrated hydrocarbons (pyrobitumen) and/or veins consisting largely of pyrobitumen, and massive organic-rich mudstones (asphalt spills/mud volcanos) are observed throughout the Zaonega Formation (Melezhik et al., 1999a). Beside C_{org}-rich mudstones and petrified hydrocarbons, known also as shungite rock, the organic-rich mudstones and dolostones of Zaonega Formation host one of the first appearances of globally significant phosphorites (Lepland et al., 2014). Phosphate precipitation in Zaonega sediments was possibly mediated by large sulphur-oxidizing bacteria living at anoxic-(sub)oxic sediment-water interfaces (Lepland et al., 2014) like in modern phosphogenetic sites at up-welling shelves off Namibia and Peru, and possibly in other ancient phosphorites (Bailey et al., 2013; Goldhammer et al., 2010; Schulz and Schulz, 2005).

Phosphorite bearing succession of the Zaonega Formations is composed of alternating C_{org}-rich mudstone - dolostone/limestone - chert sequences. Mudstone occurs as thin laminae to several meters thick flat-laminated packages. The thin laminated mudstones are interpreted as microbial mats (Lepland et al., 2014), and thick packages might represent background mud sedimentation under hydrodynamically calm conditions (Črne et al., 2012a, b). Carbonate rocks and the cherts occur in this interval as massive rock. Melezhik et al. (1999a) distinguished two main lithological types of dolostone in Zaonega Formation: dolostone megaconcretions and sedimentary dolostone. The dolostone megaconcretions were described as lensoidal, massive, C_{org}-rich, black, fine- to medium-grained secondary rock without internal structure, whereas the sedimentary dolostones were described as primary laminated

grey C_{org}-poor or black C_{org}-rich lenses or thin beds. Alternatively, Črne et al. (2012b) suggested that the massive appearance of the dolostones might be the result of recrystallisation and megaconcretions can be of sedimentary, diagenetic, hydrothermal, metasomatic or multigenetic origin.

The formation of chert beds in the Zaonega Formation seems to be equally complicated as of carbonates. The chert in Zaonega Formation appears as a black, massive rock with a conchoidal fracture. Melezhik et al. (1999a) described it as a cloudy textured chert with a fine crystalline groundmass exhibiting no lamination, and possibly as a primary siliceous chemical sediment. However, Črne et al. (2012a) suggested, that although some chert intervals show lamination and could represent primary seafloor precipitates, then massive chert might be of secondary origin evidencing the postdepositional mobilisation of silica.

Phanerozoic cherts (siliceous deposits) are dominantly of biogenic origin (Maliva et al., 1989) and derived through diagenetic recrystallization of amorphous silica tests of phyto- and zooplanctic muds(oozes) during burial to microcrystalline chert through an opal-CT intermediary (Kastner et al., 1977; Maliva et al., 1989; Maliva et al., 2005). However, origin of Proterozoic chert is still an unresolved question (Siever, 1992) and considered to be of inorganic origin (Maliva et al., 1989), though the mechanisms of their formation e.g. via direct precipitation (Posth et al., 2008; Ramseyer et al., 2013) or diagenetic-hydrothermal replacement is poorly understood (Maliva et al., 2005).

In this thesis I report a petrographical-mineralogical-chemical study of the chert-mudstone-dolostone units in the upper, phosphorite bearing, sequence of the Zaonega Formation. The overall aim of the study is to reveal the secondary diagenetic/hydrothermal and/or primary sedimentary origin of chert and massive dolostone units.

Geological setting

The Zaonega Formation in the Onega Basin is located in the south-eastern part of the Archean Karelian craton in NW Russia (Figure 1). The sequence of low metamorphic-grade, volcano-sedimentary rocks of the Onega Structure lies unconformably on Archean granites and gneisses. The succession dips 10-50º filling a large, NW-SE-trending synform, which is covered by Palaeozoic sedimentary rocks south of Lake Onega. The Paleoproterozoic rocks underwent deformation and greenschist-facies metamorphism during the Svecofennian orogeny at 1.89 - 1.79 Ga (Melezhik et al., 1999a; Ojakangas et al., 2001).

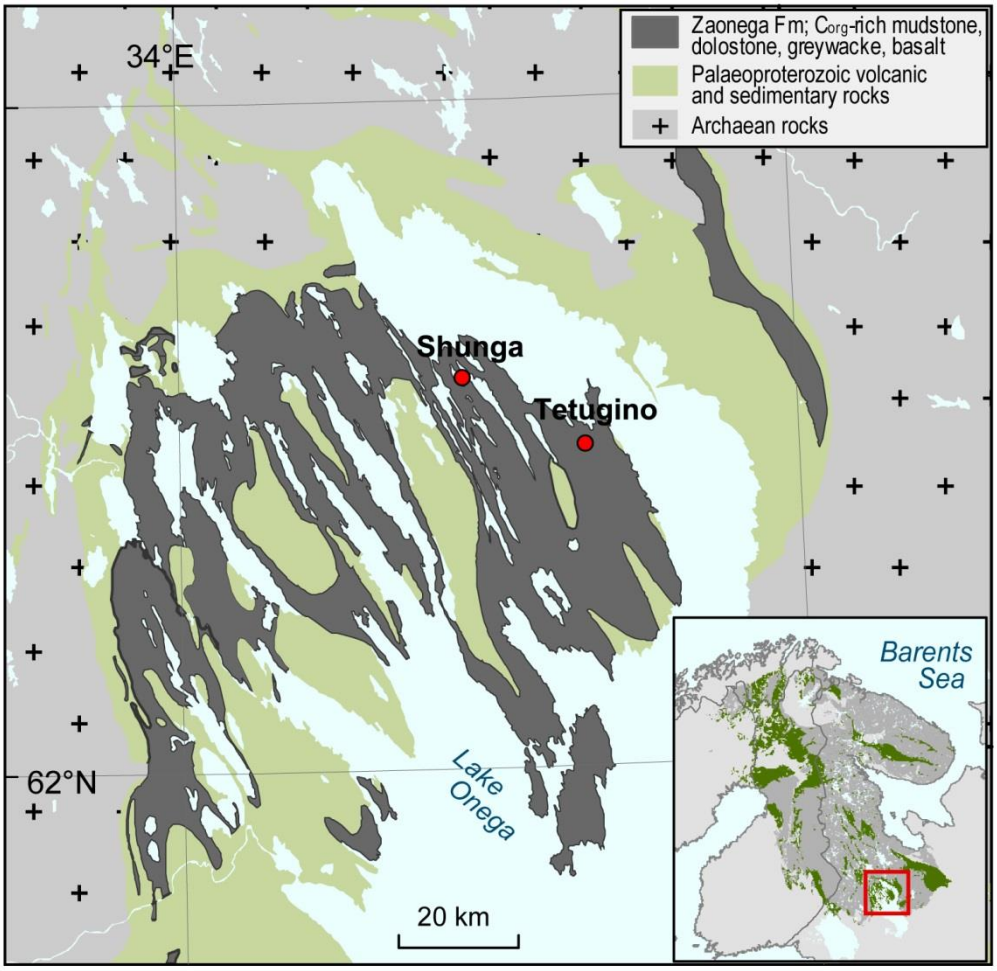

Figure 1. Simplified geological map of the Onega Basin, Karelia, Russia (according to Aivo Lepland, personal communication).

The Paleoproterozoic rocks of the Onega Basin are subdivided into four super-horizons - the Sarioli, Jatuli, Ludicovi and Kalevi. The Ludicovian Super-Horizon is subdivided into two lithostratigraphical units. The lower horizon is defined as the Zaonega Horizon and the upper

part as Suisari Horizon. These units correspond to the Zaonega and Suisari formations, respectively (Melezhik et al., 1999a; Melezhik et al., 2012).

The several hundreds of meters thick Zaonega Formation represents a succession of sedimentologically immature siliciclastic rocks, limestones, dolostones, cherts, mafic tuffs and basalts, which are all intruded by gabbroic sills (Črne et al., 2012b). Peperite contacts of sills and surrounding sediments indicate that the gabbro was intruded while the sediment was still soft and wet. The Zaonega sequence occurs above the Tulomozero Formation, which is dominated by carbonate rocks characterized by positive carbon isotope signature known as Lomagundi-Jatuli excursion (Karhu and Holland, 1996; Melezhik et al., 1999b) whereas the Suisari Formation basalts and gabbroic sills overlie it (Črne et al., 2012b). The sedimentary rocks of the Zaonega Formation are particularly rich in organic carbon reaching >40% in massive organic-rich (mudstone) units and >90% in pyrobitumen veins (Melezhik et al., 1999a; Melezhik et al., 2004). Organic-rich mudstone and dolostone beds also contain several phosphorous-rich layers in upper part of the Zaonega Formation (Lepland et al., 2014). The maximum age of the Zaonega Formation is the Pb-Pb age of 2.09 Ga, which is determined for dolostones of the underlying Tulomozero Formation (Ovchinnikova et al., 2007). The minimum Sm-Nd and Pb-Pb combined mineral and whole-rock isochron age of ca. 1.98 Ga is obtained from a mafic-ultramafic sill of the overlying Suisari Formation (Puchtel et al., 1999).

The organic material in the Zaonega formation has been referred to as shungite, which forms a black, dense, amorphous or nanocrystalline mass consisting of $C_{org,}$ with an average value of 25% (max 98%). The carbonaceous material occurs as autochtonous kerogen residues and allochtonous pyrobitumen. The shungite source rocks were originally deposited in an intraplate rift setting, while syncronous volcanism and hydrothermal activity enhanced sedimentation and nutrient delivery favoring the high degree of preservation of organic material (Črne et al., 2012b). The range of $\delta^{13}C_{org}$ values of -45‰ to -17‰ suggests a biological origin of the carbon, which was later altered by diagenetic and metamorphic processes (Melezhik et al., 1999a; Melezhik et al., 2004). A Raman spectroscopy study by van Zuilen et al. (2012) suggests that the carbonaceous material in these rocks experienced a peak temperature between 360 ºC and 400 ºC during the greenschist metamorphism.

Materials and methods

The samples for this study were collected in three outcrops of the shungite-bearing rocks in the northeastern part of the Onega Structure, Karelia (Figure 1) during fieldwork in October 2012 and July 2013. The best known outcrop of shungite-bearing rocks is near the village of Shunga (62º35´32" N 34º55´38" E). Although the exact stratigraphic position of the exposed succession is uncertain, it is believed to represent the upper part of the Zaonega Formation (Melezhik et al., 1999a; Melezhik et al., 2004). The organic-rich rock unit consists of organic-rich mudstones, dolostones and thin layers of pyrobitumen, which are overlain by a bed of C_{org}-rich chert with numerous dolostone megaconcretions (Figure 2a, b). The sequence also contains elevated concentrations of phosphate in the mudstone-dolostone interval. These phosphates consist mainly of fluorapatite, phlogopite and carbonaceous matter, forming impure layers, lenses and nodules (Lepland et al., 2014).

Another area where the upper Zaonega Formation rocks are exposed is approximately 20 km southeast form Shunga in Tetugino village (Figure 1). There are two smaller outcrops only a couple hundred meters apart. The first outcrop is exposed in an exploration excavation made in the year 2012. This succession exhibits organic-rich mudstones, dolostones, chert and some phosphate rich intervals (Figure 2d). The second outcrop exposes a C_{org}-rich chert bed with dolostone megaconcretions (Figure 2c).

Altogether 25 samples representing chert, dolostone megaconcretions, mudstone and dolostone beds were collected (Table 1). From the collection of samples chert and dolostone contacts from Shunga and Tetugino, and a profile of mudstone-dolostone-chert in Tetugino were chosen for detailed analysis. Additionally, four polished thick sections, previously prepared by Aivo Lepland and Lauri Joosu at Geological Survey of Norway (NGU), were chosen as representing a mudstone-dolostone-mudstone interval in Shunga outcrop (Figure 3).

Figure 2. Outcrops of the shungite-bearing rocks in the Onega Structure. a) The Shunga village outcrop. b) A carbonate concretion in massive chert from Shunga outcrop. Stacked line indicates location of the carbonate concretion and white dots the sampling locations. c) Tetugino outcrop exposing a C_{org}-rich chert bed. Stacked line outlines dolostone megaconcretions and approximate sample locations. d) Tetugino exploration excavation exposing a mudstone-dolostone-chert interval, dolostone bed is outlined with a stacked line.

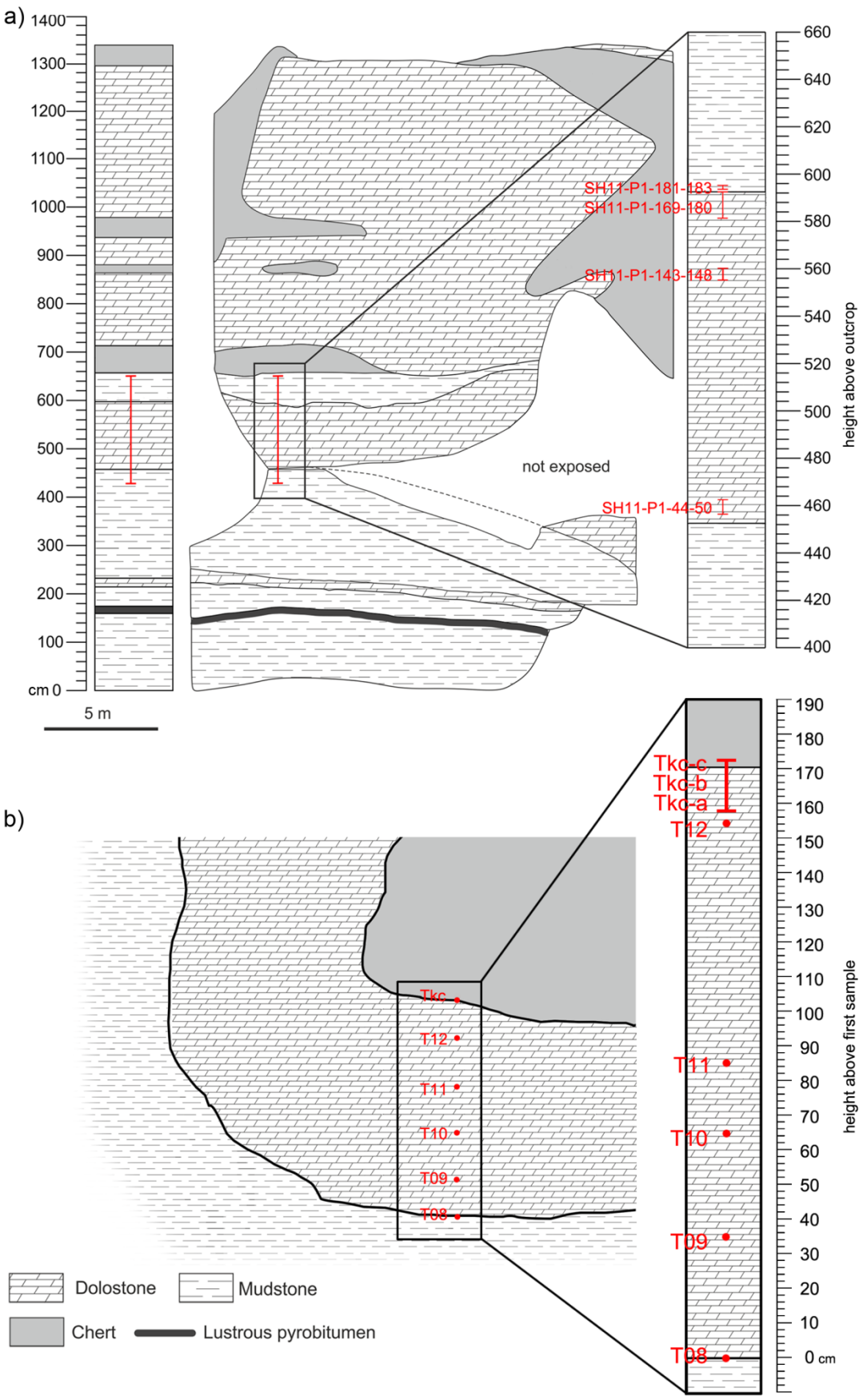

Figure 3. Lithological profiles of a) Shunga village outcrop after Joosu et al. (submitted) and b) mudstone-dolostone-chert interval from the upper part of the Tetugino excavation. Sample locations are shown in red.

Table 1. Sample identification and description.

Sample name	Location	Type	Description
SH01	Sunga outcrop	carbonate and chert contact	The margin of a carbonate concretion, on the road side of the outcrop.
SH02	Shunga outcrop	carbonate	Same carbonate concretion as SH01, on the road side of the outcrop.
SH13-03	Shunga outcrop	chert	On the right side of the outcrop, near chert and dolostone concretion contact.
SH13-04	Shunga outcrop	carbonate	On the right side of the outcrop near chert and dolostone concretion contact.
SH11-P1-44-50	Shunga outcrop	mudstone and carbonate contact	Near the lower mudstone-dolostone bed contact.
SH11-P1-143-148	Shunga outcrop	carbonate	Dolostone bed.
SH11-P1-169-180	Shunga outcrop	carbonate	Dolostone bed.
SH11-P1-181-183	Shunga outcrop	mudstone and carbonate contact	Upper dolostone bed-mudstone contact.
SHchert	Shunga outcrop	massive chert	Massive chert from the outcrop.
T08	Tetugino	mudstone and carbonate contact	Mudstone-dolostone bed contact from the exploration ditc, 0 cm marker.
T09	Tetugino	carbonate	35-45 cm from the lower contact (sample T08).
T10	Tetugino	carbonate	65-75 cm from the lower contact (sample T08).
T11	Tetugino	carbonate	75-85 cm from the lower contact (sample T08).
T12	Tetugino	carbonate	120-125 cm from the lower contact (sample T08).
Tkc	Tetugino	caronate and chert contact	155-170 cm from the lower contact (sample T08), dolostone bed-chert contact.
T13	Tetugino	carbonate	Carbonate concretion from the second Tetugino outcrop.
T14	Tetugino	carbonate	Same carbonate concretion as T13.
T15	Tetugino	carbonate	Carbonate concretion.
T16	Tetugino	carbonate	Same carbonate concretion as T15.
T17	Tetugino	laminated chert	Tetugino outcrop, loose boulder.
Tchert	Tetugino	laminated chert	Tetugino outcrop, loose boulder.

For petrographic analysis the samples were embedded in epoxy resin and polished slabs were prepared. The petrographic characterization was performed by means of optical microscope and scanning electron microscope (SEM) analysis. For optical microscopy Leica DM2500P polarization microscope equipped with Leica DFC495 digital camera in reflected light mode was used. SEM imaging of uncoated samples was done using a ZEISS EVO MA15 SEM in variable pressure mode. The images were captured by backscattered electron (BSE) and variable pressure secondary electron (VPSE) mode. To complement the SEM imaging, chemical characterization by elemental mapping of the samples was performed with Oxford AZTEC-MAX energy-dispersive spectroscopy (EDS) analysis. The use of uncoated specimens in VPSE mode allowed producing charge contrast images (CCI) for sample

characterization. CCI is an imaging mode, which allows imaging variations in crystal defect distribution (Robertson et al., 2005; Watt et al., 2000).

Major element composition was analysed by X-ray fluorescence spectrometry (XRF) using a Rigaku Primus II XRF spectrometer using pressed powder pellets. Mineralogical composition was measured in powdered unoriented samples with a Bruker Advance D8 powder X-ray diffractometer and interpreted-analysed by Peeter Somelar.

Carbon and oxygen stable isotope analyses were done to observe the differences in isotopic composition in the mudstone-dolostone-chert transitions. Small amounts of samples were drilled, using a minidrill, from the surface of 6 polished slabs from Shunga and Tetugino. Grinded whole rock powders were used for the Tetugino profile samples. Stable carbon and oxygen isotopes were measured with a Thermo Delta V Advance mass-spectrometer using GAS-Bench II interface. Results are reported respect to VPDB standard in permil.

Charge contrast imaging

Charge contrast imaging is a technique that allows high-resolution, high-magnification imaging of conductivity differences in uncoated geological samples in variable pressure scanning electron microscope (VP SEM). Principally SEM images are collected from signals arising from bombardment of a sample with an electron beam. Due to the electron bombardment conventional high-vacuum SEM induces a negative charge on the sample surface and non-conductive samples begin to charge. Charging damages samples and makes it difficult to obtain high-quality images, therefore samples have to be coated with conductive materials, typically carbon, gold or platinum. Coating samples eliminates charging, but might cause artefacts and mask small scale morphological features (Robertson et al., 2005; Watt et al., 2000).

In the VP SEM a gas is introduced into the sample chamber where backscattered and secondary electrons from the sample interact with gas molecules, producing positive ions. The positive ions migrate towards the sample where they neutralize the negative charge build up. This charge neutralizing effect gives the advantage of using uncoated samples. Nevertheless, charging of the sample can occur at low chamber gas pressures, because insufficient charge balancing positive ions are produced. These low pressure conditions allow to image conductivity contrasts in different materials (Figure 4) (Robertson et al., 2005; Watt et al., 2000).

In uncoated samples different dielectric properties might cause electron trapping and charging in high-charge density areas. Charge traps are caused by defects, dislocations, impurities and vacancies in the crystal lattice, giving information about compositional and structural variations in geological samples. CCI detects defects similarly as cathodoluminescence (CL) and thus images provided by both methods have high correlation. However, CCI has a higher resolution and can be applied to a wider variety of geological samples. CCI provides images of internal growth, defect structures and relict fluid pathways in a wide range of poorly conductive samples (Griffin, 2000; Watt et al., 2000).

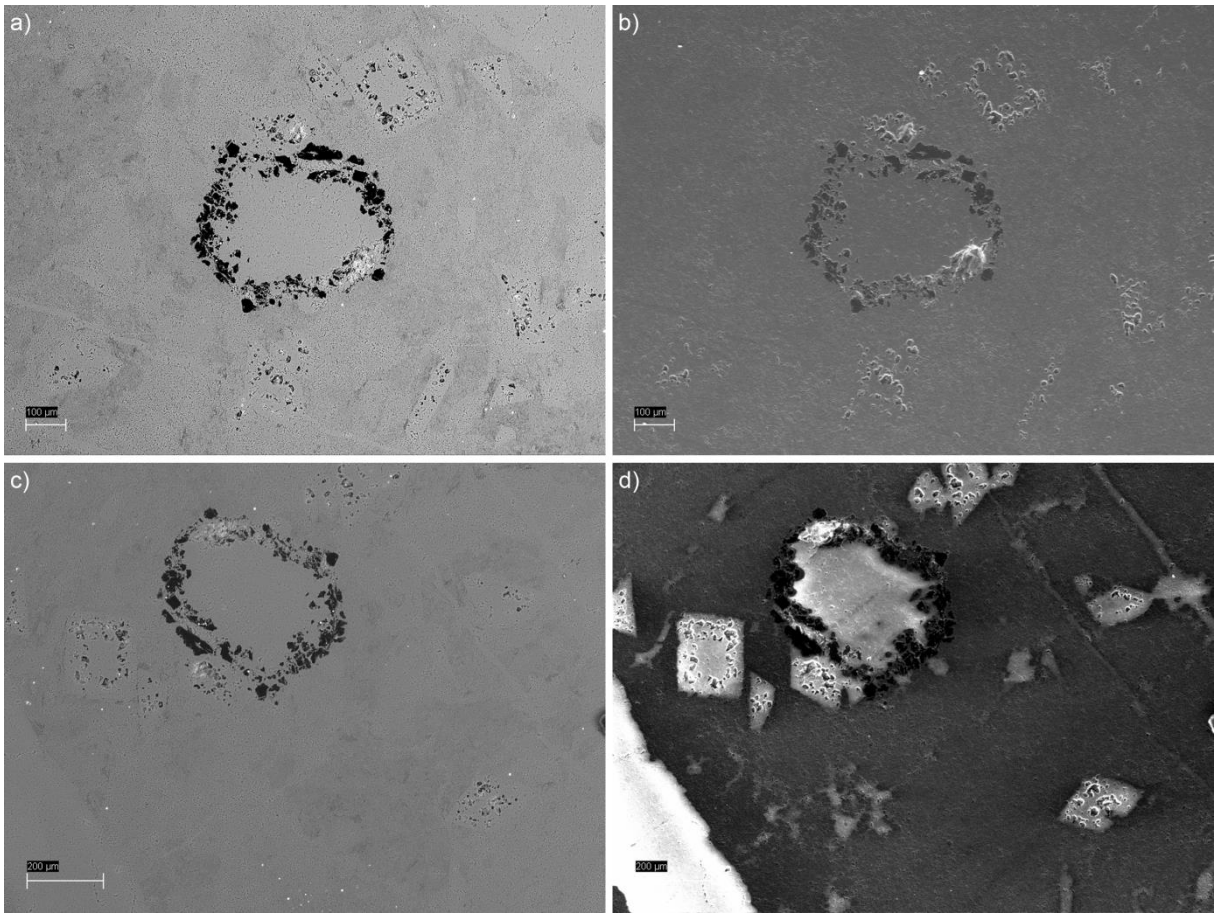

Figure 4. SEM imaging of chert (sample Tkc), a) coated sample in backscattered electron mode, b) coated sample in variable pressure secondary electron mode, c) uncoated sample in backscattered electron mode, d) uncoated sample in variable pressure secondary electron mode exhibiting charge contrast.

Results

Petrography

Chert

Chert in Shunga and Tetugino outcrops occurs as a thick bed overlying organic-rich mudstones and dolostones with numerous large carbonate inclusions (Figure 2, 3). Chert is typically black in colour, massive texture and has a conchoidal fracture (Figure 5a). Exceptions are two samples from Tetugino outcrop (T17, Tchert) which show subparallel to concentric lamination (Figure 5b). Massive chert has a cloudy texture and is made up of crypto- and microcrystalline quartz and dispersed minor organic matter cross-cut by quartz veinlets. Particle size of individual quartz crystals is about 2-5 μm (Figure 6). Although chert is black due to the incorporated organic matter, the content of C_{org} does not exceed typically 7%.

SEM imaging in BSE mode reveals a fuzzy pattern in the distribution of organic matter and mosaic/cloudy patterns in massive chert types, caused by agglomeration of spheroidal or polygonal quartz crystals, bounded by finely disseminated organic matter. These quartz spheroids frequently occur as aggregates and are ~10-20 μm in diameter, mostly spherical and in some cases polygonal (hexagonal) in shape. Element mapping with SEM-EDS shows only spectra for Si, O and C (Figure 7 a, b, c, 8) whose distribution corresponds to generally uniformly cloudy texture of the rock.

However, in variable pressure SEM mode with charge contrast imaging in some areas appear, where nebulous brighter structures or quartz veins become visible (Figures 7a, b). The spheroidal aggregates have mostly no charge contrast, but rarely minor contrast occurs in the centers of the polygonal aggregates (Figure 8). Most interestingly, in some cases charge contrast imaging of the chert exhibits rhombic shapes with higher charging within otherwise chemically indistinctly uniform chert (Figure 7a, b).

“Laminated” chert is characterized by wavy patterns of black and light-grey transitional layers of about ~1-2 mm thick. Chert layers show spheroidal aggregates, lenses and patches of quartz crystal aggregates and finely disseminated, abundant, cloudy-looking organic matter (Figure 7c). The layering is caused by rhythmically higher share organic carbon (Figure 7c). The laminated chert is cross-cut by quartz veinlets.

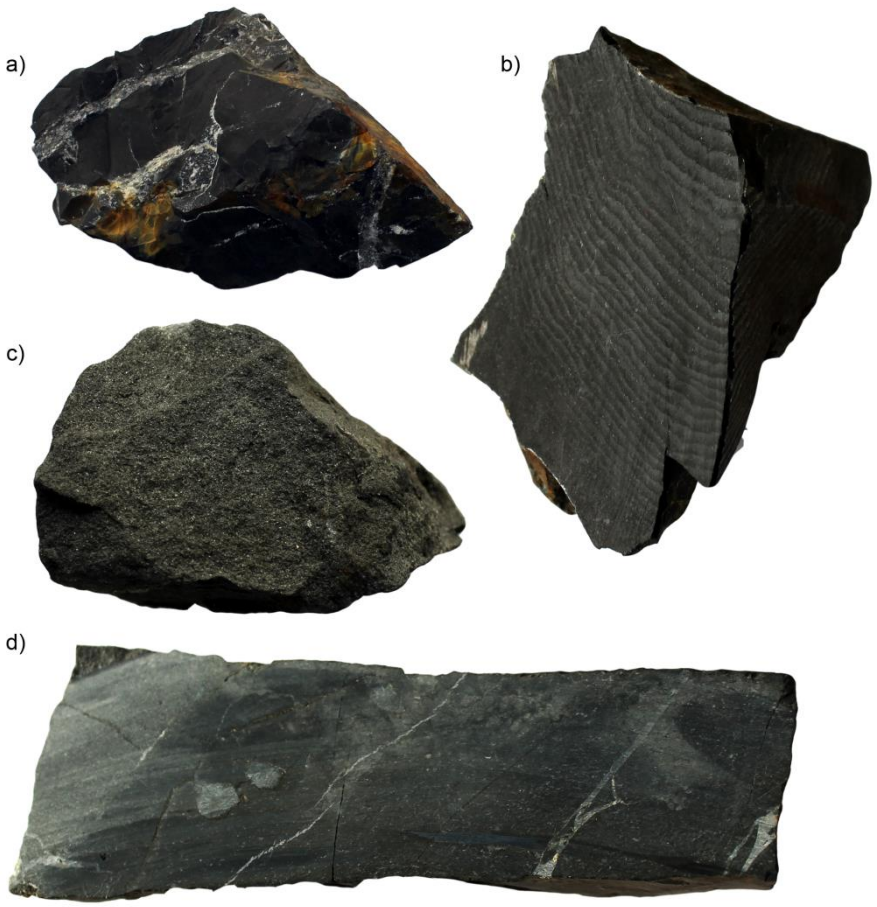

Figure 5. Hand specimens from Shunga and Tetugino. a) Massive chert from Shunga outcrop (sample SH13-03). b) "Laminated" chert from Tetugino (sample Tchert). c) Dolostone bed sample from Tetugino excavation (sample T11). d) Dolostone concretion and chert contact from Tetugino outcrop (sample T16).

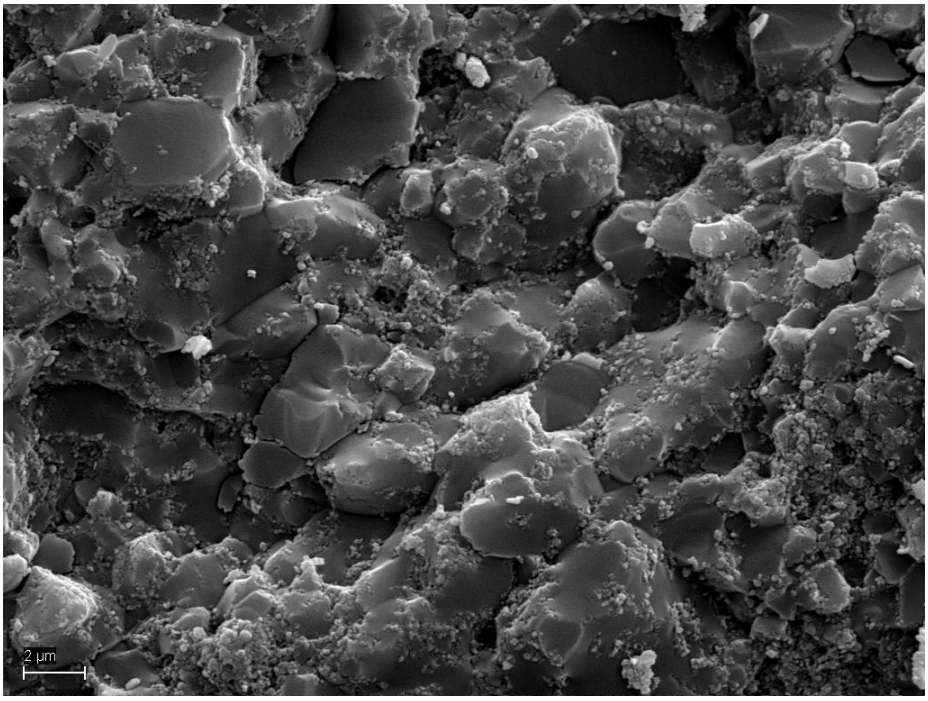

Figure 6. High-vacuum SEM image of a chert sample. Particle size of individual quartz crystals is ~2-5 µm.

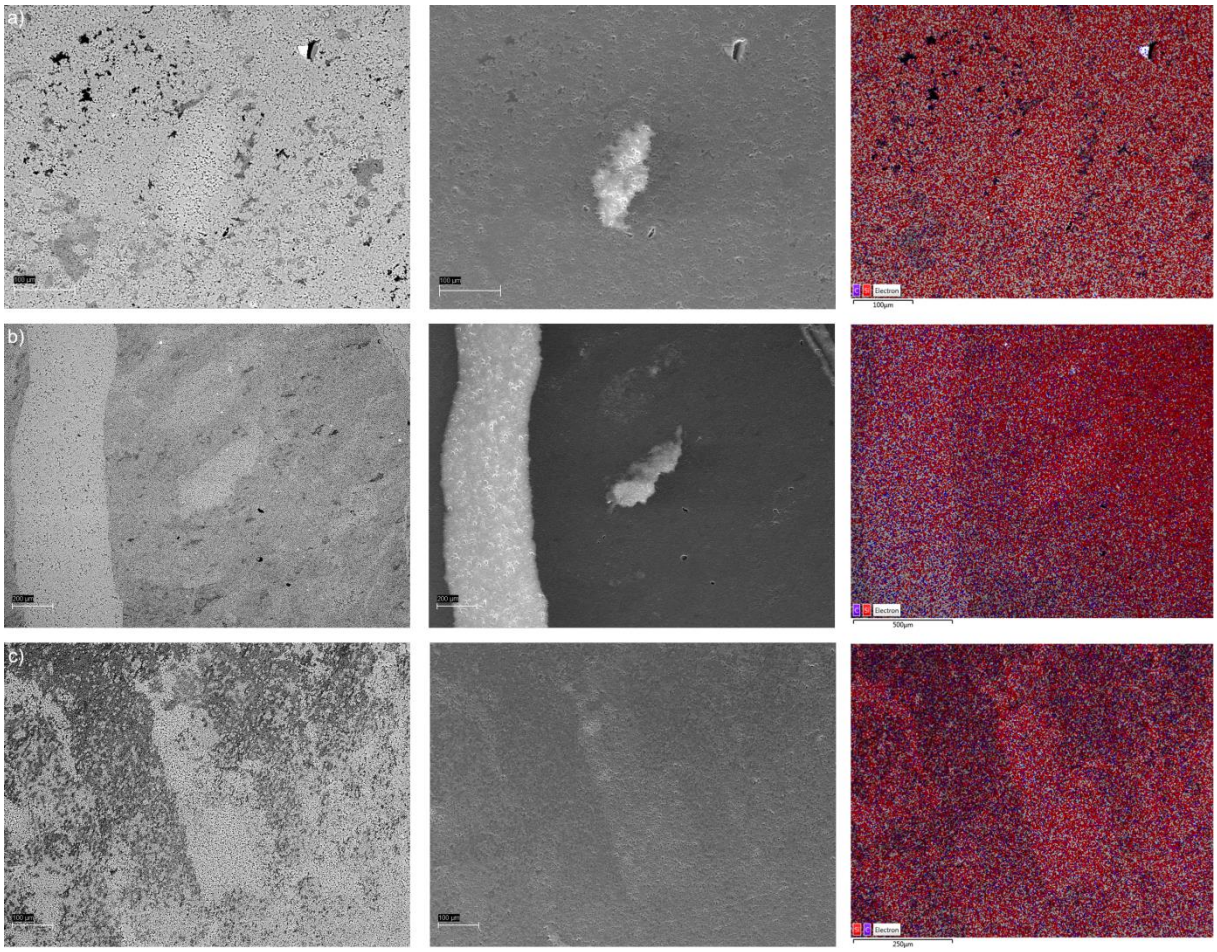

Figure 7. SEM imaging of chert in BSE mode (left), charge contrast imaging (middle) and element mapping with EDS (right). a) Massive chert sample SH13-03 from Shunga. b) Massive chert sample SHchert from Shunga. c) "Laminated" chert sample T17 from Tetugino.

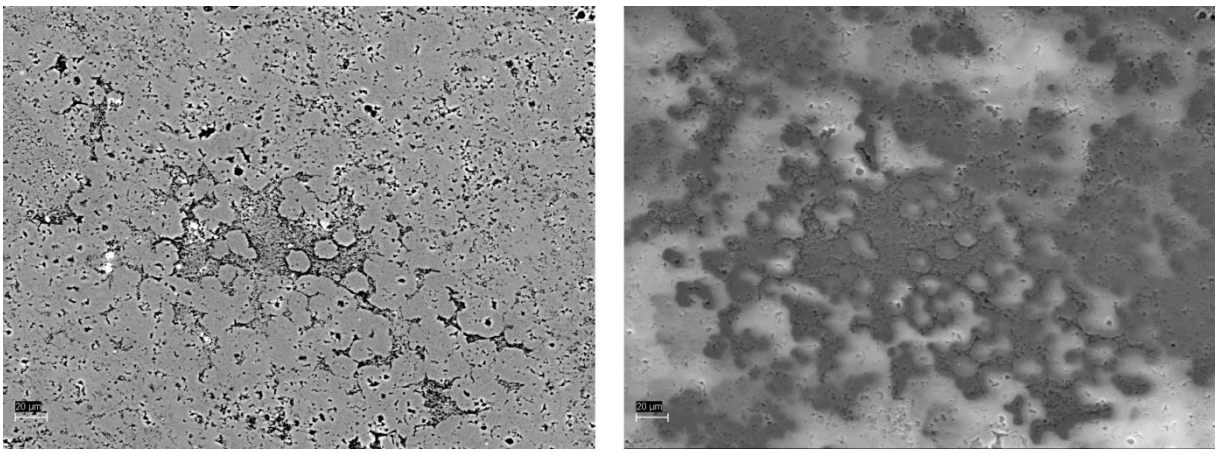

Figure 8. Polygonal and spheroidal aggregates in chert. Minor charge contrast occurs in the centers of the polygonal aggregates. BSE image on the left and charge contrast image on the right.

Dolostone

Previously Melezhik et al. (1999a) distinguished two lithological types of dolostone, namely dolostone megaconcretions and sedimentary dolostone. We studied both varieties of these dolostones from Shunga and Tetugino outcrops, where dolostones occurs as layers overlain by mudstone or chert beds and as concretions in chert (Figure 2, 3)

Dolostone in the Shunga and Tetugino profiles is grey or dark grey and medium-grained (Figure 5c). Tetugino dolostone bed has no internal structure, in contrast to the Shunga dolostone bed that shows weak layering. Centers of the beds (samples T11, SH11-P1-143-148) comprise mainly of large (ca. 100 μm in size) tightly packed subhedral dolomite crystals (Figure 9b, 10b). Sample SH11-P1-143-148 from Shunga outcrop (see for position Figure 3a) shows more tightly intergrown crystal aggregates and shapes of individual crystals are difficult to recognize. Sample T11 has minor quartz in its composition, whereas SH11-P1-143-148 contains apatite, calcite, quartz and mica (Figure 9b). These mineral phases are typically tightly intergrown. Dolomite crystals are mostly homogenous in BSE images with slightly brighter spots. These brighter areas contain according to EDS analysis higher Ca content, possibly indicating some dedolomitization. VPSE charge contrast imaging reveals zonal dolomite crystals and strong charge contrast of the dolomite aggregates (Figure 10b, 11b, c).

The dolostone "megaconcretions" *sensu* Melezhik et al. (1999a) within chert bed are ellipsoidal in shape, massive, dark grey and medium-grained (Figure 2b, c, 5d). The megaconcretions contain large and mostly rhombohedral dolomite crystals (Figure 11c, 14b, c). Central parts of the concretions comprise, compared with the margins, of more tightly packed euhedral to subhedral dolomite crystals (Figure 11c, 12c). In the interstices of the dolomite crystals quartz, apatite and mica occur. Some dolomite crystals reveal quartz rims (Figure 11b, c) and BSE imagery shows brighter more Ca-rich patches inside the dolomite crystals (Figure 11b, c).

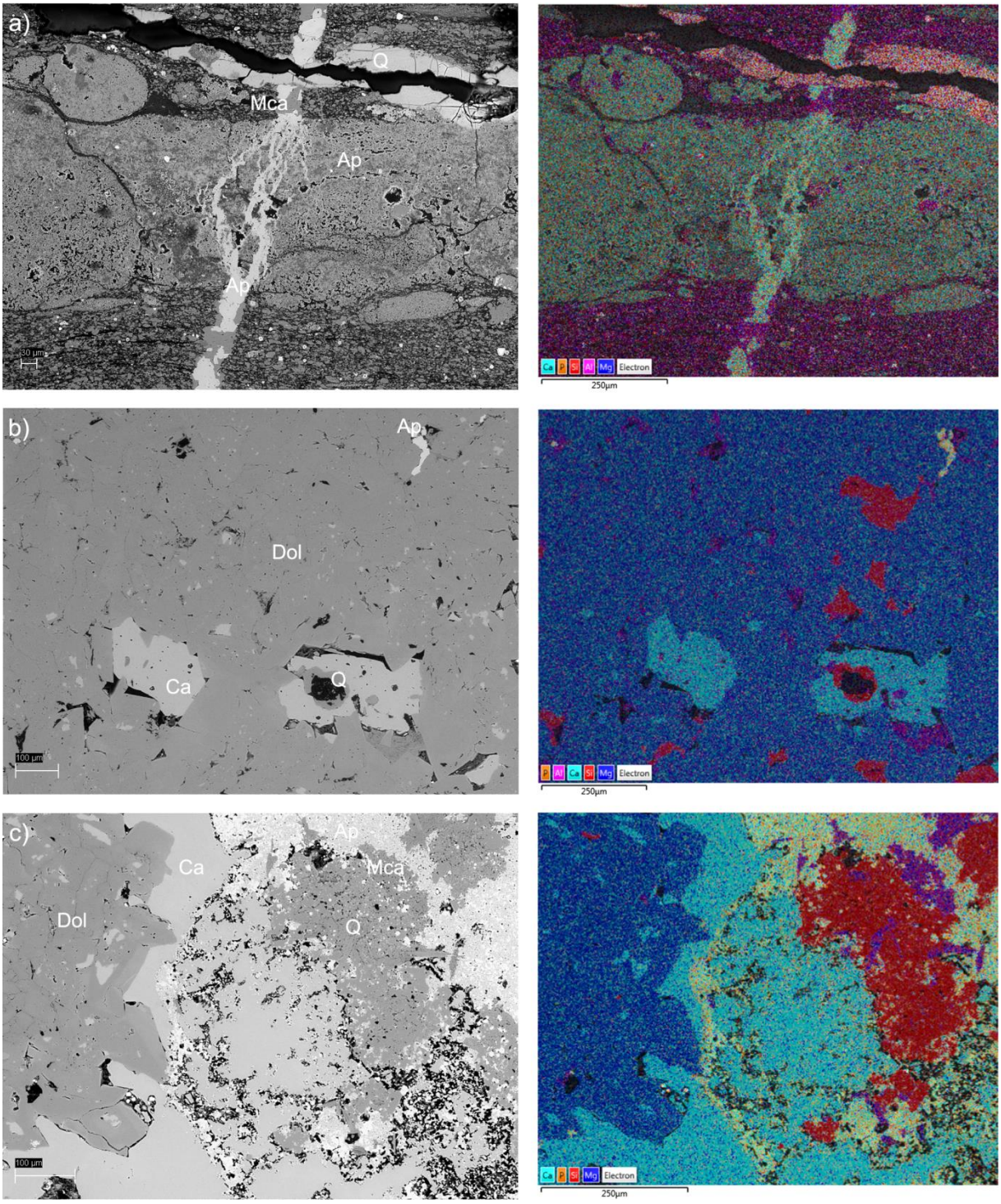

Figure 9. Mudstone-dolostone-mudstone profile from Shunga village outcrop. BSE images on the left and element mapping on the right. a) Upper mudstone contact (sample SH11-P1-181-183), b) centre of the dolostone bed (sample SH11-P1-143-148), c) dolostone near the lower mudstone contact (sample SH11-P1-44-50).

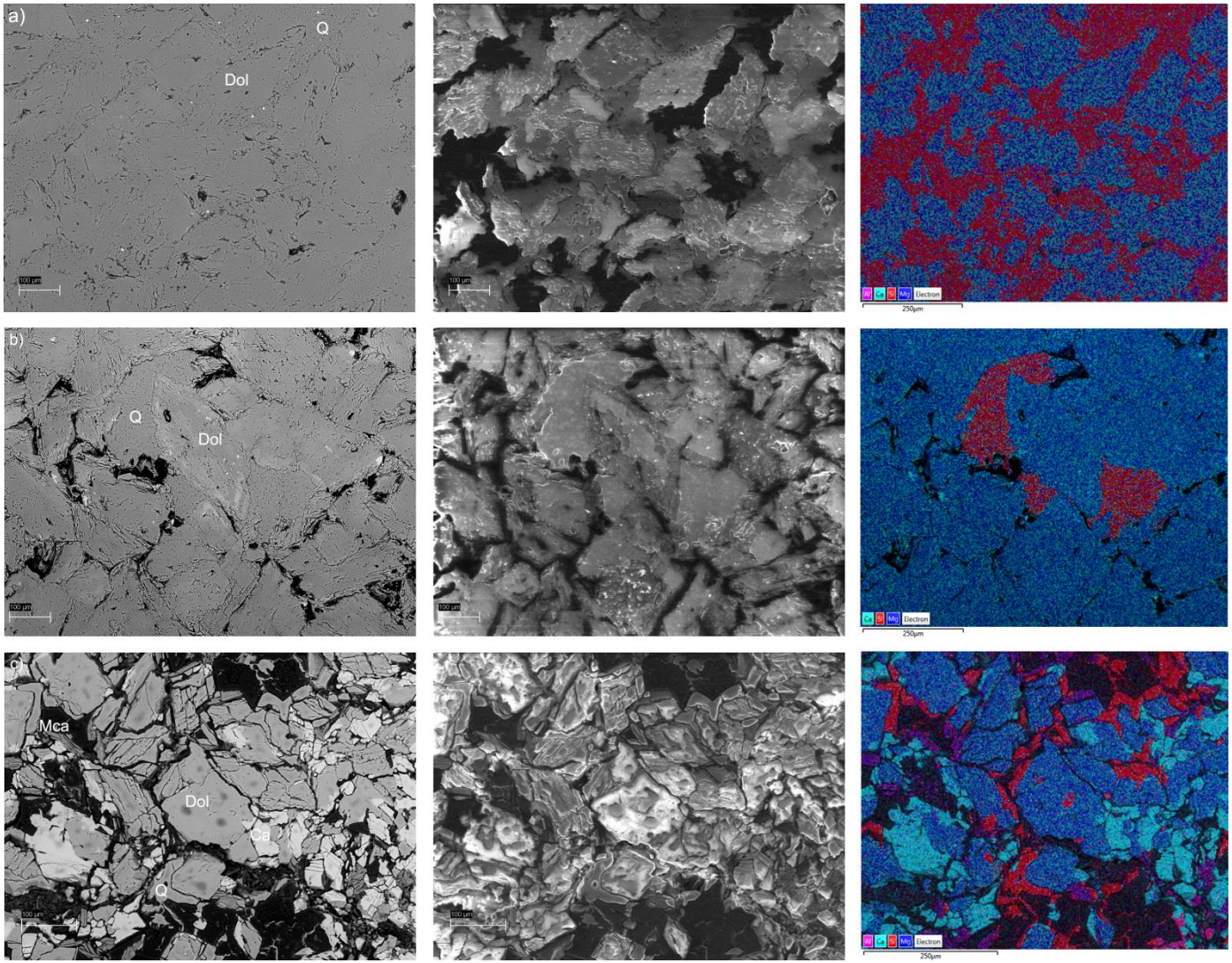

Figure 10. Mudstone-dolostone-chert profile from Tetugino excavation. BSE images on the left, charge contrast images in the middle and element mapping on the right. a) Upper chert contact (sample Tkc), b) centre of the dolostone bed (sample T11), c) lower mudstone-dolostone contact (sample T08).

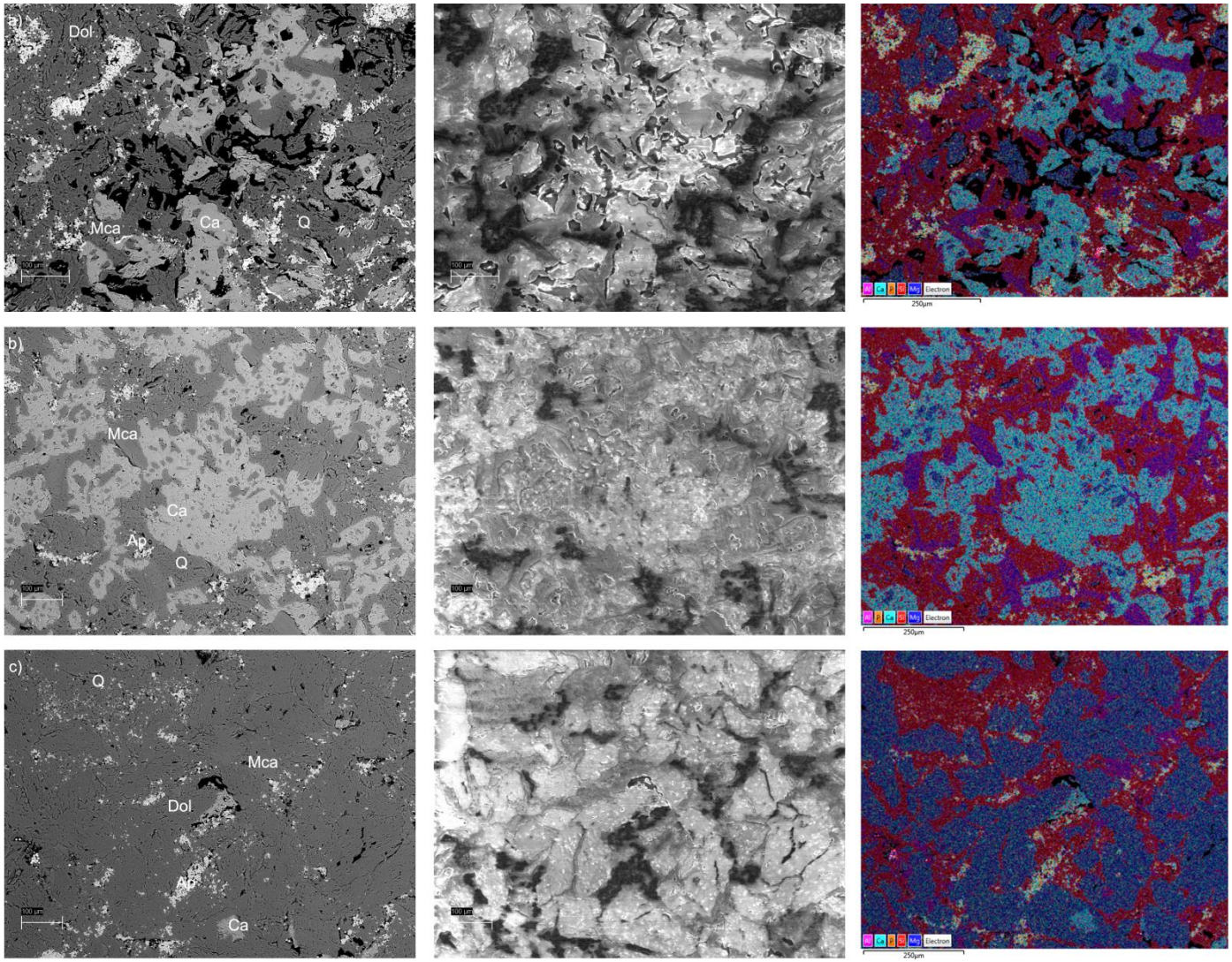

Figure 11. Carbonate concretion from massive chert (sample T15). BSE images on the left, charge contrast images in the middle and element mapping on the right. Moving from the margin (a) towards the centre part of the concretion (b) and (c).

Contact zones

Contacts between chert and dolostone concretions are typically gradual, whereas the dolomite content decreases and quartz increases towards the contact zones (Figure 5d, 11). In some cases the contacts are rather sharp and rimmed by large calcite crystals, which occasionally have preserved dolomitic cores (Figures 12b). Also the margins of the concretions contain occasional large irregularly shaped or rhombohedral calcite crystals with numerous relict dolomite inclusions. Calcite is typically tightly intergrown with apatite, quartz and mica. In some cases irregular calcite crystals have a quartz-mica rim with a rhombohedral shape.

Quartz, apatite and mica are more abundant at the margins of the concretions compared with central parts. Apatite crystals are mostly tightly intergrown with calcite, but also occur in the intercrystalline space of the chert masses, outlining rhombohedral shapes (Figure 12a). Mica often occurs with quartz, apatite and calcite, forming crystal aggregates in the interstices of dolomite and calcite crystals, rims around dolomite crystals or replacement structures with rhombohedral shape in the contact zone.

The margins of the Shunga dolostone bed are characterized mostly by tightly intergrown dolomite crystals with recognizable rhombohedral shape. While the main carbonate phase is dolomite, quartz, calcite, mica and apatite are more abundant compared with middle parts of the beds. The central parts of dolomite crystals are darker in BSE images and brighter patches appear at the margins. EDS mapping reveals that these brighter areas are more Ca-rich (Figure 9b, c, 10b, 12c, 14b, c). The lower mudstone-dolostone contact of the Tetugino profile is composed of calcite and organic matter, but quartz, dolomite and mica phase (phlogopite) are also abundant. Subhedral dolomite crystals form clusters and have rims composed of quartz, calcite and mica (Figure 15a, b). Organic matter occurs in the intercrystalline space, sometimes forming spheroidal structures in association with quartz (Figure 10c, 15c, d).

Dolostone-chert and mudstone-dolostone contacts show peculiar replacement structures. Most clearly are distinguished silica pseudomorphs after dolomite (Figure 12a, b, 13a, b, 14a). In the contact zones the chert imaging in BSE mode, and more effectively with charge contrast imaging, reveals bright rhombohedral areas. In places these bright shapes enclose relict isolated crystals of dolomite. Near the contacts the charge contrast images show rhombohedral shapes mostly with sharp outlines, but further away from the contact zone these outlines become more irregular and fuzzy. Some chert samples also contain dolomite crystal moulds, where sometimes dolomite relicts have been preserved (Figures 13a, b, 14a).

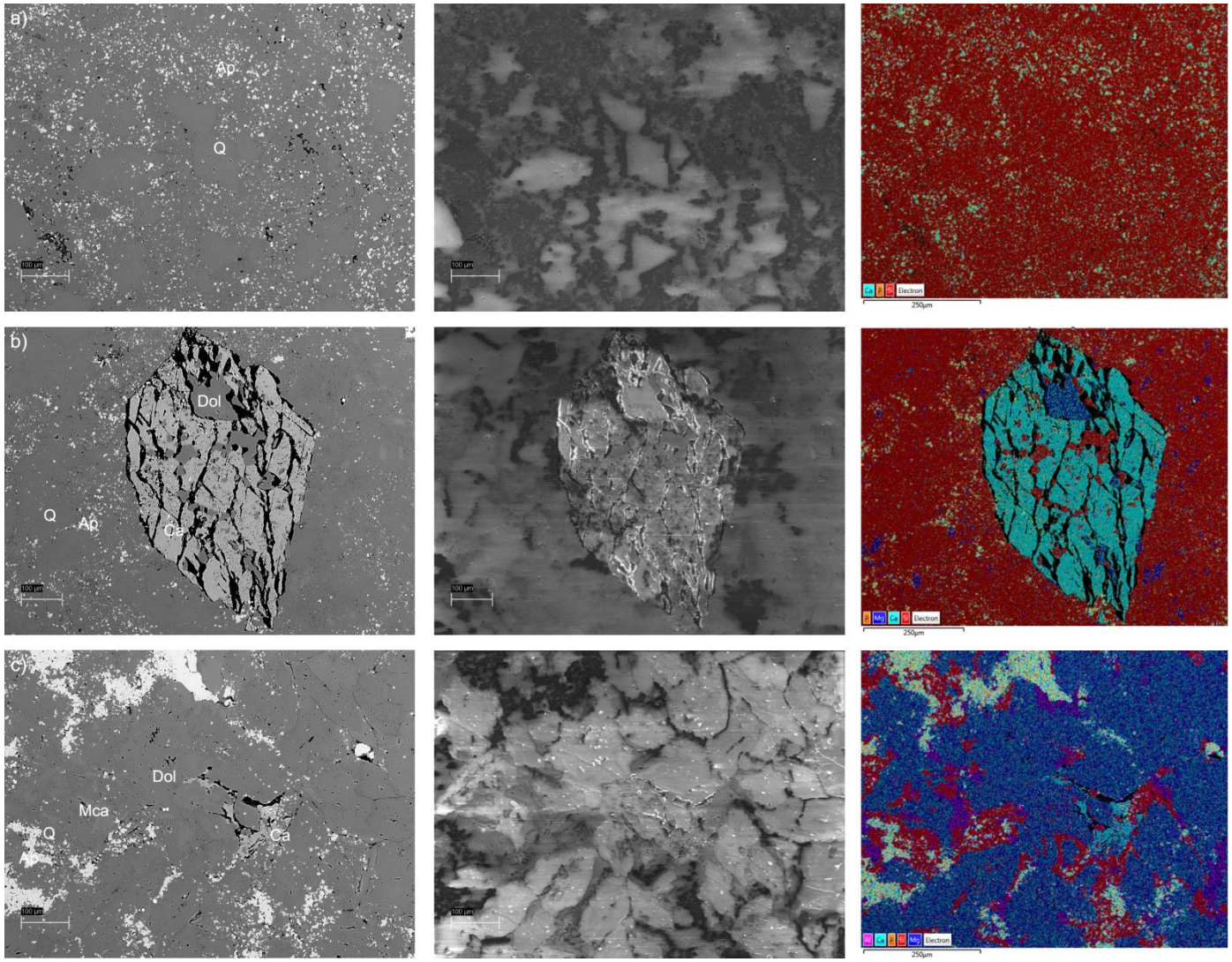

Figure 12. Contact between chert and a dolostone concretion (sample T16). BSE images on the left, charge contrast images in the middle and element mapping on the right. a) Chert from the contact zone. b) Large calcite crystals at the contact with chert. c) Dolostone in the vicinity of the contact zone.

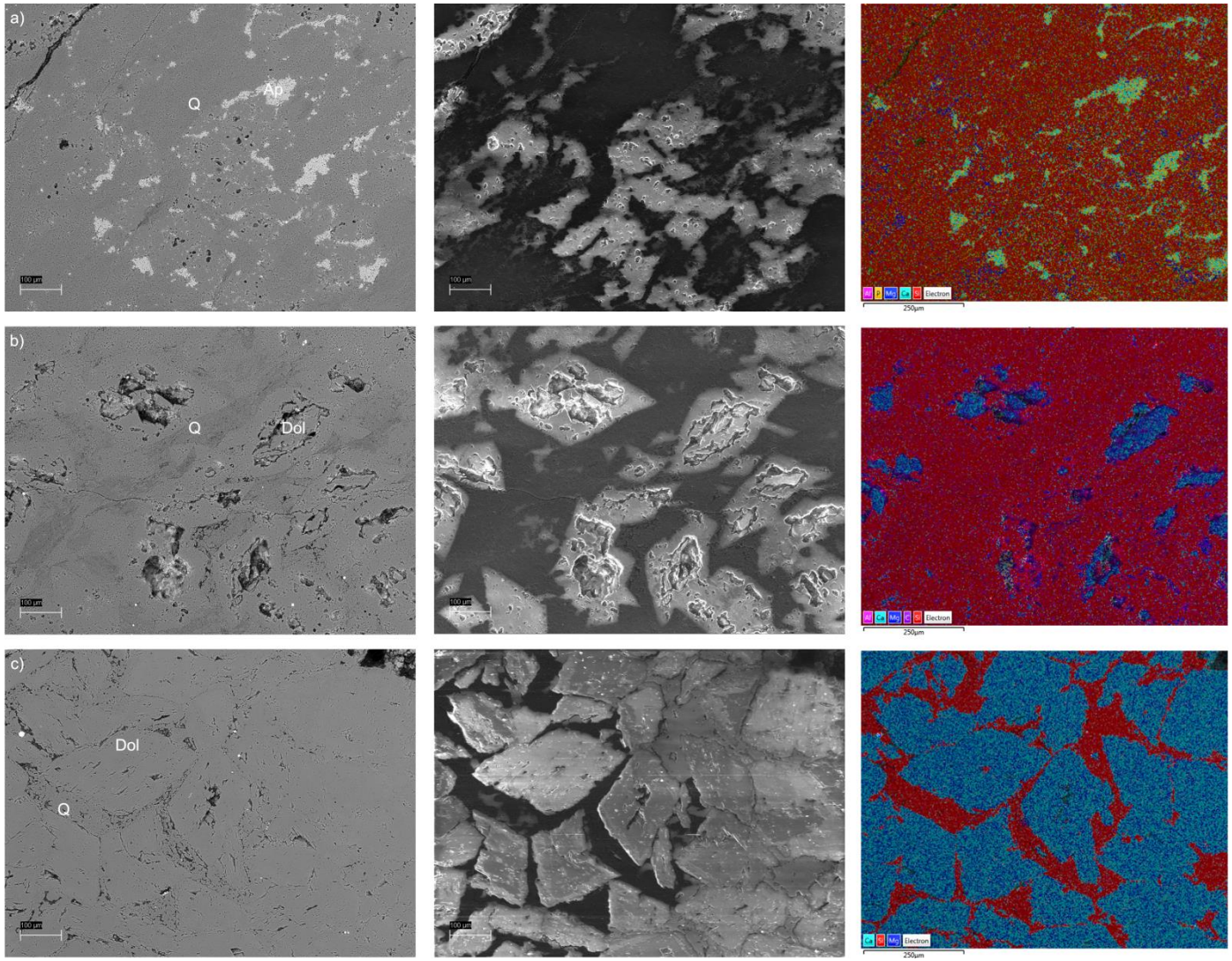

Figure 13. Contact between chert and a dolostone bed (sample Tkc). BSE images on the left, charge contrast images in the middle and element mapping on the right. a) Chert from the contact zone. b) Rhombohedral shapes in chert with enclosed relict crystals of dolomite. c) Dolostone in the vicinity of the contact zone.

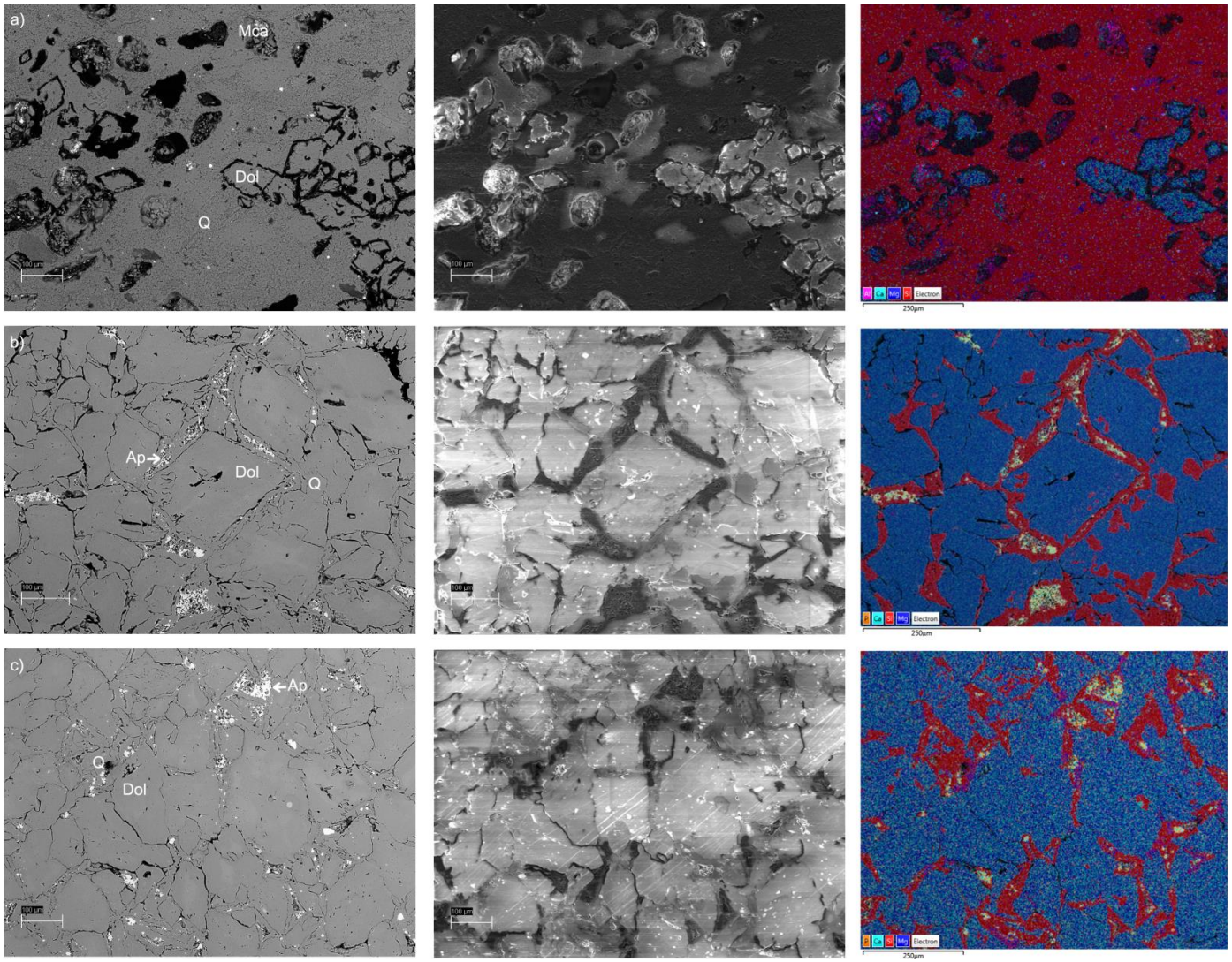

Figure 14. Contact between chert and a dolostone concretion. BSE images on the left, charge contrast images in the middle and EDS maps on the right. a) Chert from the contact zone with rhombohedral voids and dolomitic cores in places been preserved (sample SH01). b), c) Dolostone from the vicinity of the contact zone (sample SH02).

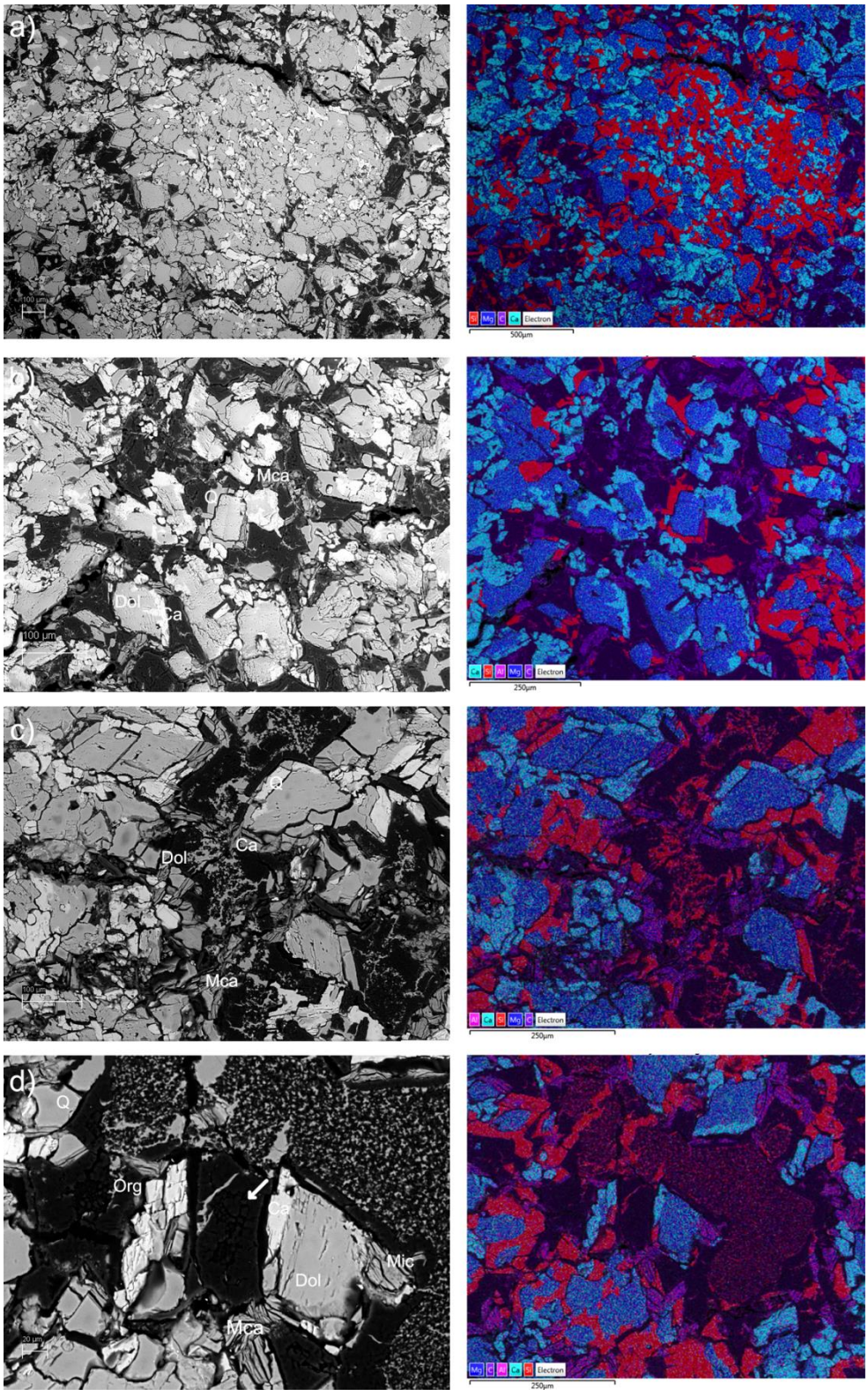

Figure 15. The lower mudstone-dolostone contact of the Tetugino profile. BSE images on the left and EDS images on the right. a) Dolomite and quartz crystals forming clusters. b) Dolomite crystals with quartz, mica and calcite rims. c) Organic matter occurs in the intercrystalline space forming structures in association with quartz. d) White arrow indicates to spheroidal structures.

Microdubiofossils

Cherts from Shunga and Tetugino contain spheroidal structures composed of quartz, which might be of biogenic origin. The spheroidal bodies have a black outer wall composed of organic matter and are silica filled. These structures occur in cryptocrystalline massive chert and are best preserved in laminated chert. Both chert types are characterized by abundant cloudy-looking black organic material (Figure 7c, 8). The spheroidal and polygonal aggregates are ~20 μm in diameter, which exceeds the minimum size for independently viable cells (Pirajno and Grey, 2002), show internal structure and they co-exist with others of similar morphology and are embedded in the rock matrix (Figure 16b, c). The outer rims of these structures are probably composed of the same organic material as the finely disseminated matter scattered throughout the chert.

Some of the silicic aggregates have black cores (Figure 16c), which may have formed as quartz crystals nucleated around a grain of organic material and the finely disseminated organic particles were pushed outwards by crystal growth along a crystal front (Pirajno and Grey, 2002). Other polygonal structures observed in chert might be pseudomorphs after apatite crystals (Figure 16a, b). These polygonal aggregates contain apatite inclusions and have a hexagonal shape, all of which support an apatitic precursor of these structures.

However, the spheroidal and polygonal aggregates found in the studied cherts satisfy some of the criteria for biogenicity (Buick, 1990) as features on figures 8, 16b, 16c. In this case, they may be replacements of fossil microorganisms. Similar spheroids have been reported previously from the Killara Formation in the Paleoproterozoic Bartle Member by Pirajno and Grey (2002). Alternatively, these features could represent dissolution cavities/voids in original dolostone that were filled with migrating hydrocarbons during oil generation (Victor Melezhik, personal communication 2014). Until further, more systematic research, we cannot classify these structures as microfossils and they must be regarded as microdubiofossils in the sense of Hofmann (1987).

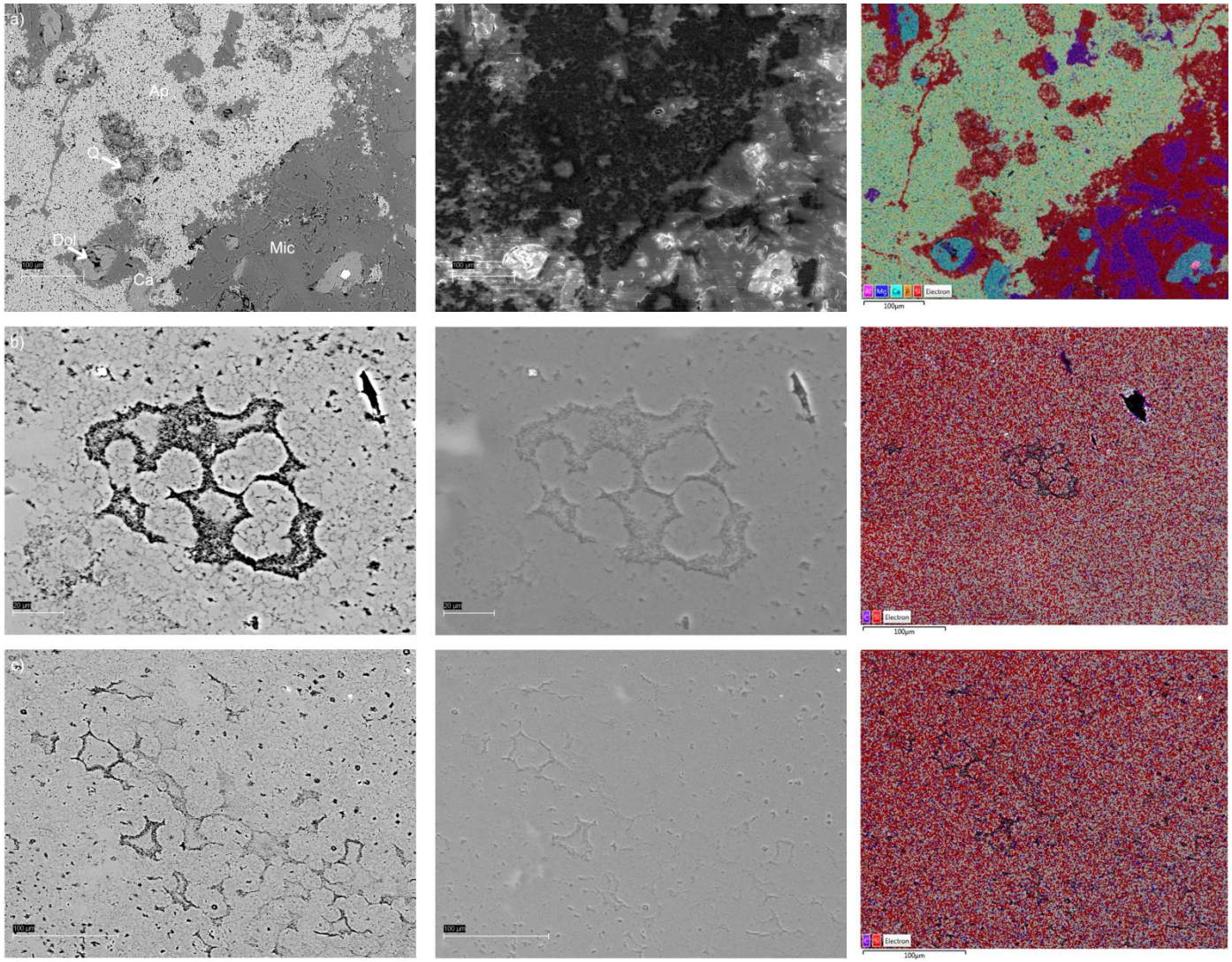

Figure 16. Spheroidal and polygonal structures from the Shunga and Tetugino outcrops. a) Polygonal structures with apatite inclusions in a carbonate concretion (sample T14). b) Spheroidal aggregates are best preserved in laminated chert (Sample T17). c) Spheroidal aggregates with black cores (sample T17).

Mineralogy and chemistry

Results of chemical and mineralogical analyses are reported in Tables 2 and 3, and shown in figures 17, 18, 19 and 20.

XRD analyses show that mineral composition of chert samples from all outcrops are composed of >90% quartz. Some chert samples near contacts with dolostone contain also minor phlogopite mica, apatite and/or talc. Mudstone units are mainly composed of phlogopite mica, minor quartz and organic material. Mudstone and dolostone contacts (e,g, sample T08) are comprised of calcite, vermiculite (high-charge smectite), organic material and some quartz and dolomite. The main carbonate mineral phase is dolomite, except in one sample (T13) where calcite dominates. There is a noticeable trend of increasing calcite, quartz and apatite content towards the margins of megaconcretions. The two profiles from Tetugino and Shunga show similar trends of dolomite decrease compared to quartz, calcite and mica towards contact zones (Figure 17, 19). Apatite is the most abundant in the upper contact zone of both profiles and in the contact zones of the megaconcretions.

Major elements composition coincides with the mineralogical trends, showing MgO and CaO decrease (dolomite and calcite) towards the margins of the profiles and increase in SiO_2, Al_2O_3 (mica, quartz) and P_2O_5 (apatite) content (Figure 18, 20).

Table 2. Mineral composition, wt%.

Sample	Quartz	Dolomite	Calcite	Apatite, F-	Talc	Mica	Vermiculite	Illite/illite-smectite	Clay, mica SUM	Albite	Gypsum	Pyrite	Chlorite
SHchert	99.7											0.3	
SH01-karb	89.2	3.1			4.8	2.9			2.9				
SH01-chert	91.6				5.0	3.2			3.2				
SH02	12.8	78.7		4.2	4.3								
SH13-03	99.7											0.3	
SH13-04	14.6	78.6	1.4			2.7	0.5	1.1	4.3	0.8		0.5	
T08	18.4	10.5	57.0				14.2		14.2				
T09	6.5	83.8	7.9				0.5	1.3	1.8				
T10	4.7	87.4	3.0		3.3		0.8		0.8	0.8			
T11	0.6	95.4	0.8		1.9		0.9		0.9				
T12	8.2	82.3	5.6			0.4	0.4	1.1	1.9				
Tkc-a	26.4	69.9				3.7			3.7				
Tkc-b	93.5	2.5				4.0			4.0				
Tkc-c	93.1	1.0		1.5		4.4			4.4				
T13	27.6	2.2	30.1	18.7		12.0			12.0		2.6	6.2	
T14	13.6	65.9	5.2	10.0		5.2			5.2				
T15	34.9	30.9	16.0	9.6		8.7			8.7				
T16-a	41.6	26.4	11.1	12.6		8.4			8.4				
T16-b	37.2	42.2	2.7	12.3		5.5			5.5				
T16-c	95.2					4.2			4.2			0.6	
T17	100.0												
Tchert	100.0												
SH11-P1-44-50	0.8	88.0	4.6	3.1	0.8	2.0			2.0	0.7			
SH11-P1-143-148	2.9	87.7	2.2	3.6	1.4	0.9			0.9	0.8			
SH11-P1-169-180	9.5	83.8	2.0	1.7	0.1	1.6			1.6	1.2			
SH11-P1-181-183	0.7			9.5		81.1			81.1	3.4			5.2

Table 3. Major element composition, wt%.

Sample	SiO_2	Al_2O_3	TiO_2	Fe_2O_3	MnO	CaO	MgO	Na_2O	K_2O	P_2O_5	S	LOI
SHchert	94.96	0.05	0.00	0.06	0.00	0.01	0.04	0.00	0.02	0.00	0.02	4.67
SH01-karb	93.15	0.12	0.00	0.20	0.01	1.18	1.42	0.00	0.07	0.02	0.03	3.60
SH01-chert	95.39	0.16	0.02	0.19	0.00	0.15	1.01	0.02	0.08	0.01	0.01	2.76
SH02	12.08	0.03	0.00	0.41	0.11	26.76	20.92	0.01	0.01	1.11	0.01	38.45
SH13-03	95.77	0.06	0.00	0.09	0.00	0.03	0.04	0.00	0.02	0.00	0.02	3.83
SH13-04	17.11	0.32	0.02	0.22	0.03	26.01	17.36	0.02	0.12	0.01	0.01	38.69
T08	16.79	1.24	0.02	0.54	0.11	29.71	6.09	0.00	0.06	0.01	0.13	45.17
T09	7.80	0.17	0.00	0.59	0.10	27.75	15.97	0.02	0.04	0.01	0.04	47.45
T10	6.66	0.19	0.01	0.82	0.10	25.93	16.67	0.02	0.02	0.02	0.05	49.39
T11	1.50	0.18	0.01	0.51	0.08	30.33	20.55	0.02	0.01	0.04	0.01	46.70
T12	10.23	0.21	0.00	0.61	0.08	28.71	16.98	0.00	0.04	0.36	0.01	42.71
Tkarb+chert-a	21.31	0.08	0.00	0.38	0.03	23.52	18.99	0.01	0.04	0.01	0.02	35.51
Tkarb+chert-b	93.78	0.25	0.01	0.17	0.00	0.59	0.84	0.00	0.12	0.04	0.02	3.95
Tkarb+chert-c	94.69	0.23	0.01	0.17	0.00	0.55	0.68	0.00	0.11	0.17	0.03	2.98
T13	37.07	2.13	0.03	4.07	0.04	26.80	5.25	0.00	0.88	5.42	0.88	16.83
T14	9.48	0.45	0.00	0.56	0.09	31.76	18.67	0.02	0.23	2.60	0.08	35.93
T15	40.02	1.46	0.03	0.77	0.05	20.98	9.50	0.00	0.64	2.51	0.02	23.61
T16-a	43.71	0.99	0.02	0.55	0.04	17.39	9.46	0.00	0.55	7.16	0.05	19.52
T16-b	38.16	0.66	0.01	0.48	0.05	21.55	10.12	0.01	0.35	5.00	0.05	23.02
T16-c	95.26	0.14	0.00	0.18	0.00	0.04	0.27	0.01	0.06	0.03	0.06	3.75
T17	97.44	0.06	0.00	0.12	0.00	0.05	0.13	0.00	0.02	0.01	0.02	2.02
Tchert	93.21	0.05	0.00	0.07	0.00	0.09	0.04	0.02	0.01	0.02	0.02	6.27
SH11-P1-44-50	3.16	0.83	0.02	0.45	0.28	29.29	19.00	0.01	0.44	0.78	0.06	45.30
SH11-P1-143-148	4.92	0.15	0.01	0.20	0.11	30.31	18.74	0.01	0.06	2.29	0.08	42.80
SH11-P1-169-180	11.11	0.54	0.01	0.44	0.32	28.88	16.17	0.01	0.25	0.75	0.06	41.10
SH11-P1-181-183	30.30	8.06	0.78	3.58	0.01	2.94	12.76	0.19	3.92	2.23	0.45	34.50

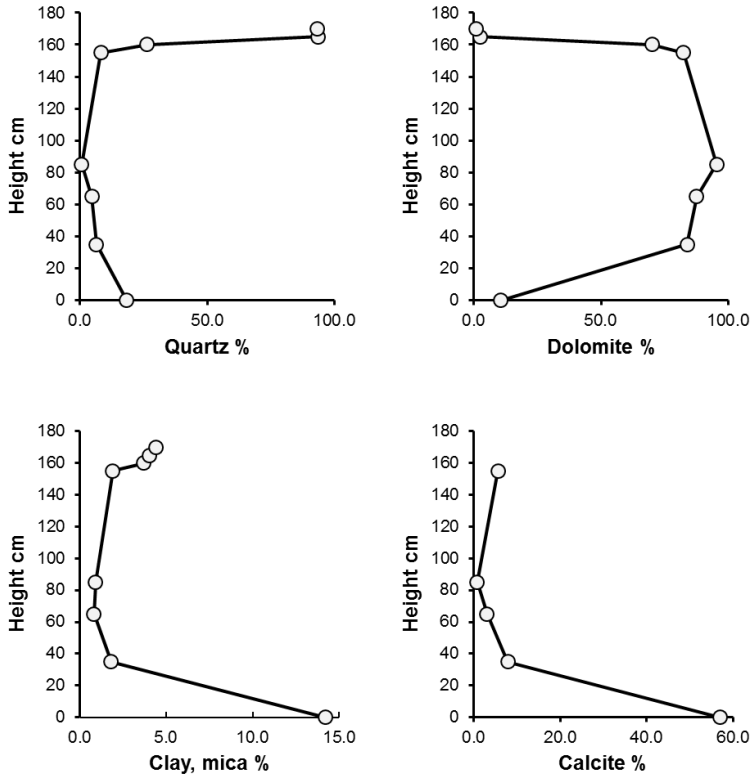

Figure 17. Major mineral trends in the mudstone – dolostone – chert profile in the Tetugino excavation. See for location of the profile Figure 3. Height is indicated as relative position above sample T08.

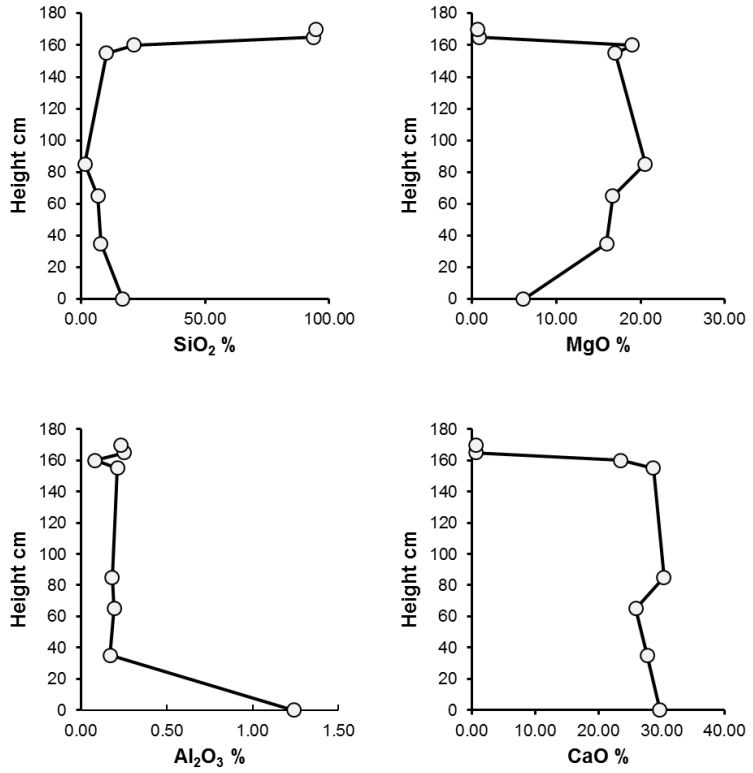

Figure 18. Major element composition trends from mudstone – dolostone – chert profile in theTetugino excavation. See for location of the profile Figure 3. Height is indicated as relative position above sample T08.

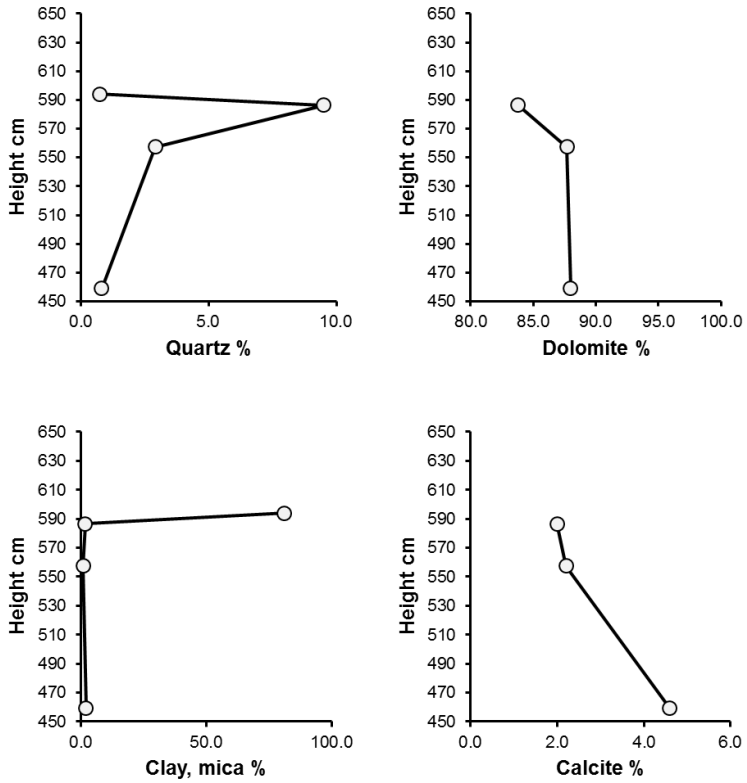

Figure 19. Major mineral trends of the dolostone –chert transition in the Shunga profile. See location in Figure 3. Height is indicated in cm above the Shunga outcrop.

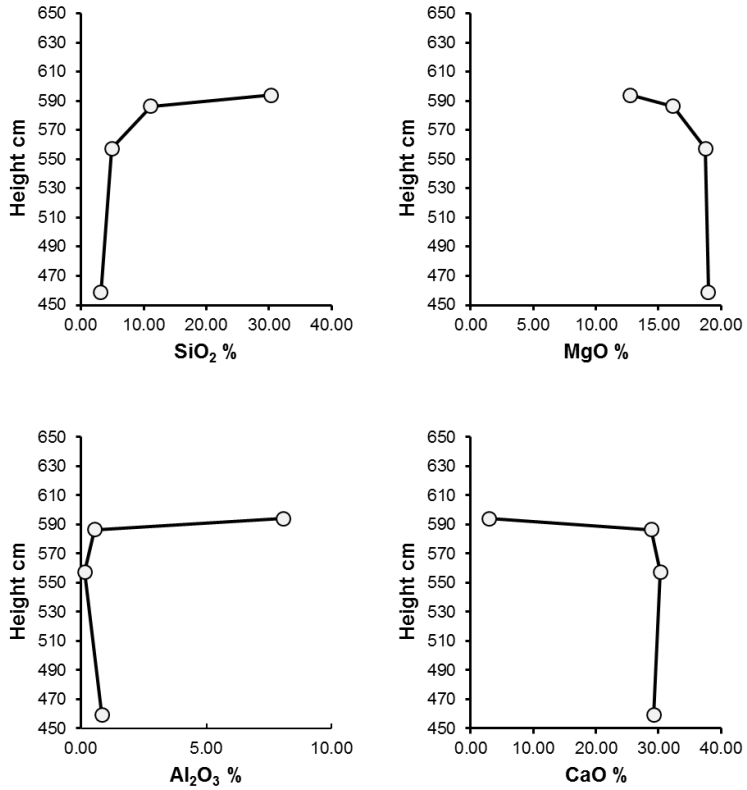

Figure 20. Major element composition of the dolostone –chert transition in the Shunga profile. See location in Figure 3. Height is indicated in cm above the Shunga outcrop.

Isotope composition

Results of carbonate carbon and oxygen stable isotope composition analyses (Table 4) show regular $\delta^{13}C$ variation at dolostone megaconcretion-chert transitions. Samples across the dolostone-chert contacts show increasing carbonate $\delta^{13}C$ values from about -15.07‰ to -3.29‰ moving further away from contacts into the dolostone (Figure 21, 22). The same trend occurs in the profiles, which display a decrease in $\delta^{13}C$ values from its central part (-4.80‰) outwards to the margins (-21.09‰) (Figure 23). Strongly depleted $\delta^{13}C$ composition of the carbonate phases indicates C_{org} source of alkalinity during the precipitation of calcite and dolomite, whereas the samples rich in calcite have more negative $\delta^{13}C$ values. The $\delta^{18}O$ values vary between -4.97‰ and -13.81‰ VPDB and show covariation with $\delta^{13}C$ values that indicates strong diagenetic influence on the $\delta^{18}O$ composition (Figure 24).

Table 4. Stable isotope composition of carbonate rocks. n.d. – low signal, not determined

Sample	**$\delta^{13}C$ ‰VPDB**	**$\delta^{18}O$ ‰ VPDB**	**Sample type**
SHO2-1	-4.78	-7.05	carbonate concretion
SHO2-2	-3.89	-6.15	carbonate concretion
SHO2-3	-3.29	-5.89	carbonate concretion
T08	-14.17	-13.43	carbonate-mudstone contact
T09	-8.86	-9.91	carbonate bed
T10	-7.35	-9.26	carbonate bed
T11	-5.36	-7.04	carbonate bed
T12	-4.80	-7.62	carbonate bed
Tkc-1	-5.98	-6.62	carbonate-chert contact
Tkc-2	-6.75	-7.95	carbonate-chert contact
Tkc-3	n.d.	n.d.	carbonate-chert contact
Tkc-4	n.d.	n.d.	carbonate-chert contact
T13-1	-11.82	-13.81	carbonate concretion
T13-2	n.d.	n.d.	carbonate concretion
T13-3	n.d.	n.d.	carbonate concretion
T14-1	-15.07	-13.35	carbonate concretion
T14-2	-14.87	-13.42	carbonate concretion
T14-3	-13.64	-13.66	carbonate concretion
T15-1	-5.53	-6.28	carbonate concretion
T15-2	n.d.	n.d.	carbonate concretion
T15-3	-4.39	-5.89	carbonate concretion
T15-4	-3.85	-5.05	carbonate concretion
T16-1	-4.33	-4.97	carbonate concretion
T16-2	-4.34	-6.39	carbonate concretion
T16-3	-7.24	-11.05	carbonate concretion
SH11-P1-44-50(72)	-7.63	-9.83	carbonate bed dolomite
SH11-P1-143-148(72)	-8.07	-10.58	carbonate bed dolomite
SH11-P1-169-180(72)	-9.52	-10.44	carbonate bed dolomite
SH11-P1-180(72)	-10.52	-8.35	carbonate bed dolomite
SH11-P1-44-50(15)	-10.20	-9.78	carbonate bed calcite
SH11-P1-143-148(15)	-9.34	-10.47	carbonate bed calcite
SH11-P1-169-180(15)	-11.98	-10.35	carbonate bed calcite
SH11-P1-180-181(15)	-21.09	-11.40	carbonate bed calcite

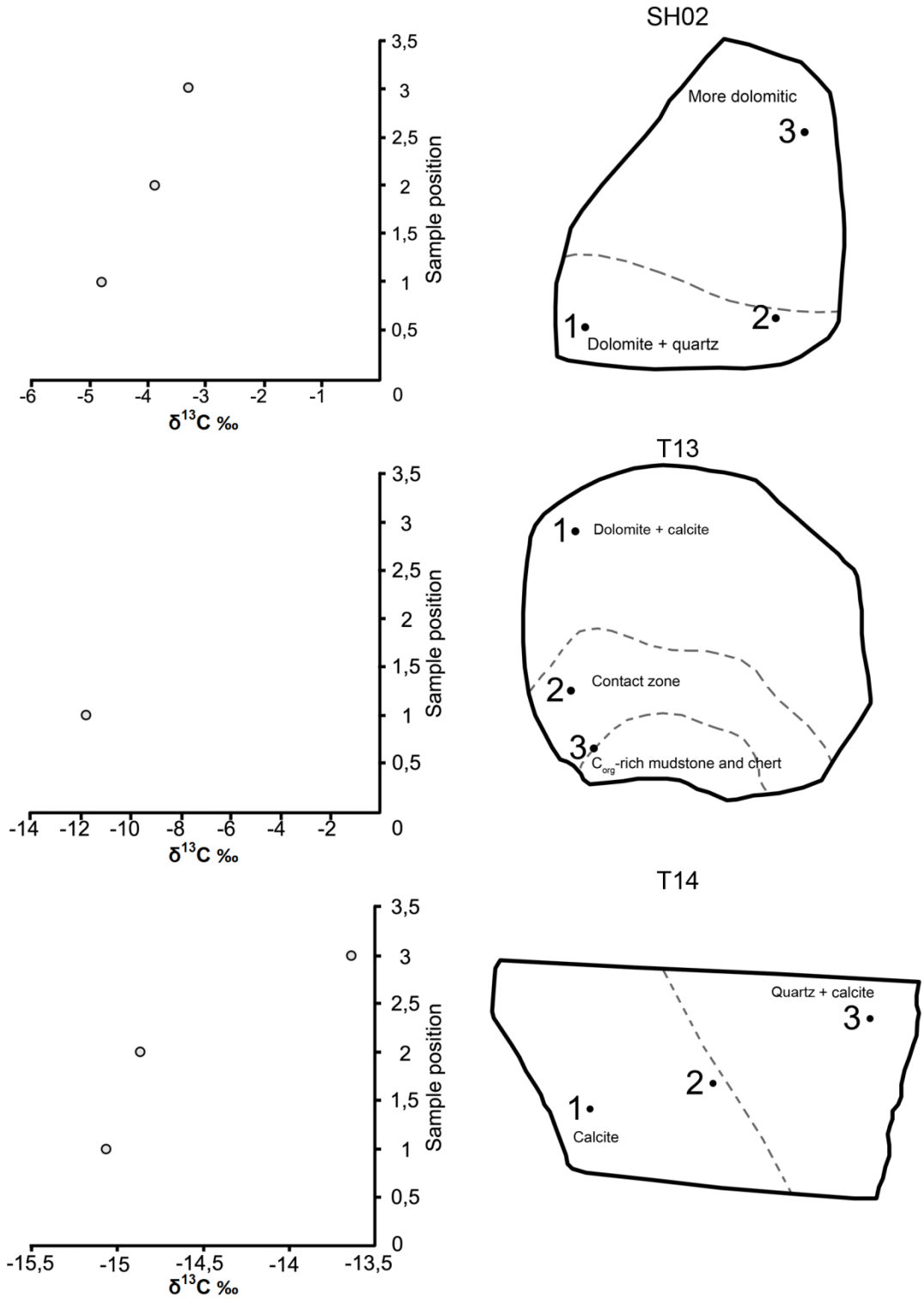

Figure 21. Distribution of $\delta^{13}C$ values in slabs made at the transition of the chert-dolostone boundaries. Black dots indicate the drilled sample position. Some drilled samples gave no $\delta^{13}C$ signal, therefore they are not shown.

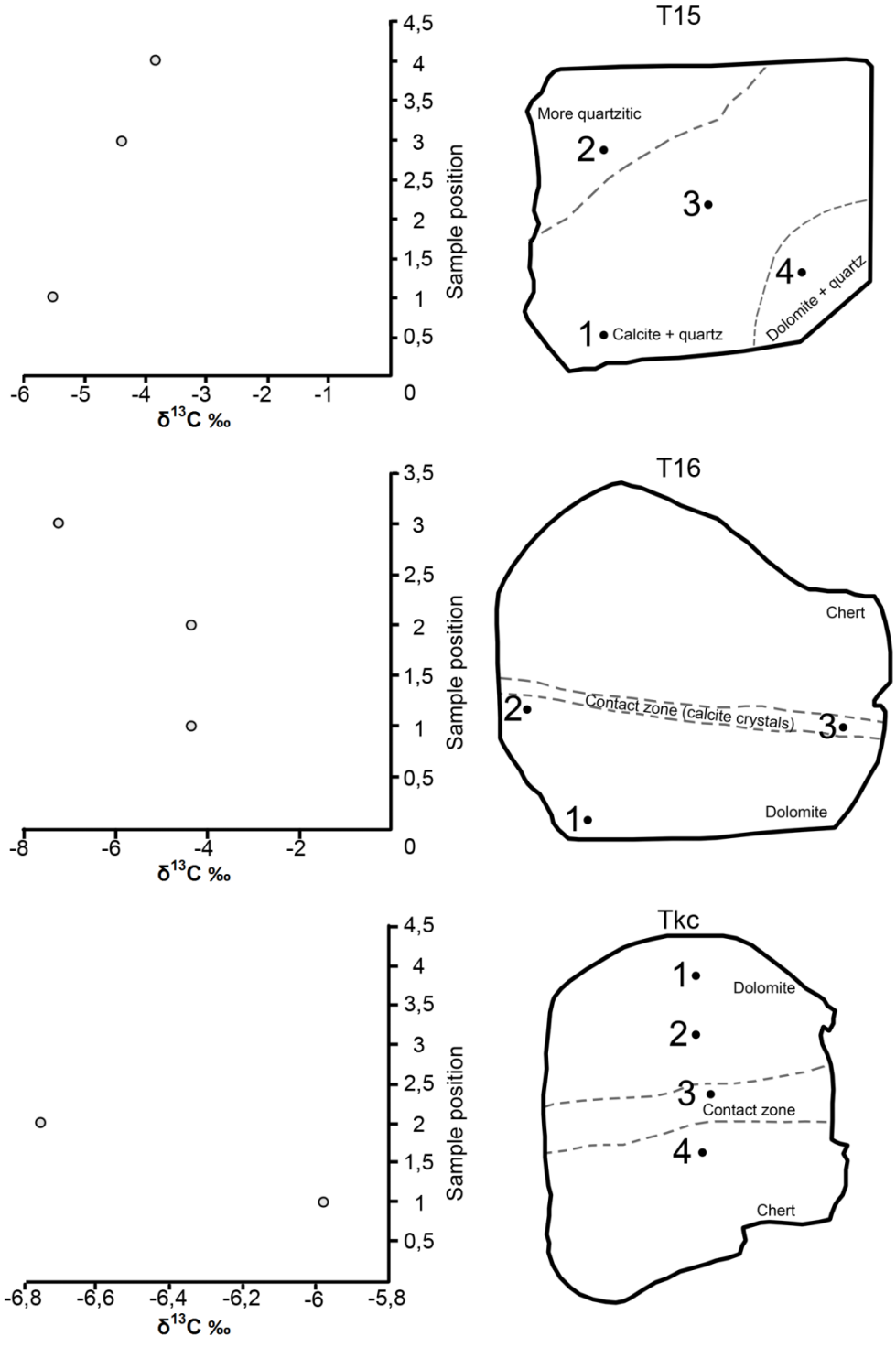

Figure 22. Distribution of $\delta^{13}C$ values in slabs made at the transition of the chert-dolostone boundaries. Black dots indicate the drilled sample position. Some drilled samples gave no $\delta^{13}C$ signal, therefore they are not shown.

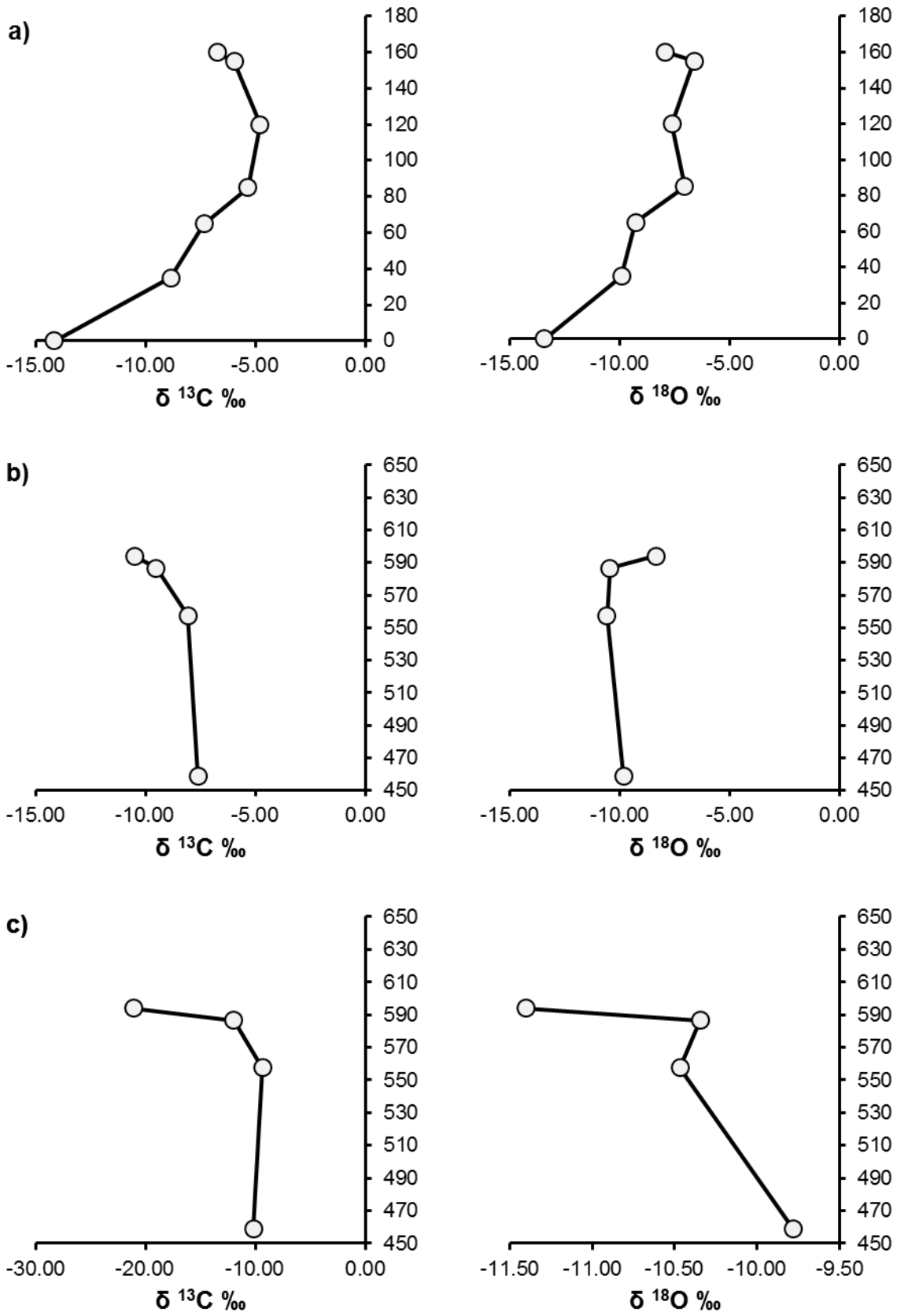

Figure 23. $\delta^{13}C$ and $\delta^{18}O$ stable isotope trends in a) Tetugino profile, b) Shunga profile dolomite, c) Shunga profile calcite. See location in Figure 3. On the Tetugino profile height is in cm above the first sample T08 and on the Shunga profile above the outcrop.

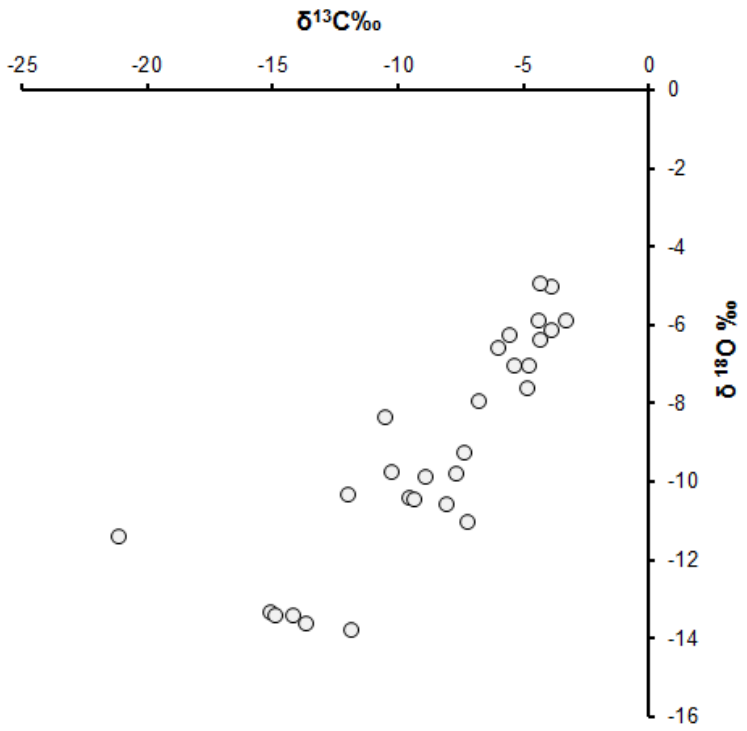

Figure 24. Covariation of the $\delta^{13}C$ VPDB and $\delta^{18}O$ VPDB values in studied samples.

Discussion

Cherts are defined as chemically precipitated hard, waxy to grainy, aphanitic sedimentary rocks composed predominantly of silica minerals. These minerals include inorganic precipitates like chalcedony and quartz, and organically precipitated opal. Besides silica polymorphs additional minerals like iron oxides, pyrite, hematite, calcite, dolomite and clays can occur in chert. The variety of accessory minerals largely depends of the associated rocks composition (Raymond, 2002).

Modern silica cycle is principally controlled by silica-secreting organisms, which precipitate amorphous silica. Phanerozoic cherts mostly form from opal-A, consisting mainly of diatom frustules, with lesser contributions from radiolarian tests and sponge spicules, which converts during diagenesis to opal-CT and gradually transforms into quartz. Modern siliceous deposits are largely constrained with deep-ocean and active continental margin basins, where primary productivity is high. Therefore shallow marine waters are undersaturated with respect to dissolved silica and cherts rarely occur. Phanerozoic nodular or bedded cherts predominantly form by late diagenetic carbonate replacement or by recrystallization of siliceous oozes (Maliva et al., 1989; Perry et al., 2005; Raymond, 2002).

In Precambrian seas significant silica-secreting biota was absent and therefore the oceans must have had higher dissolved silica concentrations, which perhaps locally reached opal-CT saturation leading to primary silicate precipitation (Maliva et al., 2005) as suggested, for example, for chert beds associated with banded iron formations and also for some laminated bedded cherts (Maliva et al., 1989; Maliva et al., 2005; Ramseyer et al., 2013). Nevertheless, Precambrian cherts are also interpreted as early diagenetic replacements of carbonates in peritidal environments (Maliva et al., 1989; Maliva et al., 2005).

The main silica source in Proterozoic and Phanerozoic is thought to be continental weathering, although their contributions to the silica cycle are different. In the Proterozoic hydrothermal circulation was more intense and thus hydrothermal fluids were a significant silica source (Chakrabarti et al., 2012; Raymond, 2002). It is difficult to find exact analogues for Precambrian cherts, but they still share similar microtextures to modern cherts (Maliva, 2001; Maliva et al., 2005).

The main Precambrian chert types are (a) early diagenetic peritidal replacement cherts, (b) late diagenetic replacement cherts, (c) banded and granular iron formation cherts deposited in deep-water environments. Peritidal early diagenetic replacement cherts occur typically within

carbonate deposits as nodules or discontinuous beds. Replacement cherts commonly preserve inclusions and ghosts of carbonate precursors and organic-walled microfossils. Such cherts are composed of microcrystalline quartz with a crystal size of ~6-8 μm. Late diagenetic carbonate replacement cherts are associated with unreplaced carbonates and have also preserved inclusions and ghosts of precursors, but microfossils are rare (Maliva et al., 2005).

Iron formation (BIF) cherts are microtexturally distinct from carbonate replacement cherts and appear to have formed by direct silica precipitation. These are composed of micro- or mesocrystalline quartz with a crystal size of ~40 μm, are not associated with unsilicified carbonate deposits, have fine-scale grain fracturing, lack carbonate inclusions or ghosts of precursors. Banded iron formations were deposited in low-energy basinal marine environments, whereas granular iron formation cherts had a high-energy subtidal deposition environment (Maliva et al., 2005).

Our results show that the Shunga and Tetugino cherts are characterized by various and abundant replacement structures: silica pseudomorphs after dolomite, relict isolated dolomite inclusions, dolomite crystal moulds, dolomite crystals with quartz or mica rims. Also, some possible microfossil remains are possibly present. Moreover, cherts in studied sections are exclusively composed of micro- or cryptocrystalline quartz with average crystallite size less than 5 μm. Therefore, from petrographical characteristics, it is evident that these chert beds did not form by direct silica precipitation, but were formed by diagenetic and/or hydrothermal replacement of dolostone sediment preserved as unsilicified dolostone beds and relicts ("megaconcretions") of the host rock within silicified sequences in Shunga and Tetugino outcrops of the Zaonega Formation.

Tectonical context of the Zaonega rocks and numerous quartz veins intersecting the sequence suggest that the silicification of the dolostone sediments was driven by hydrothermal fluids. The hydrothermal activity during Zaonega deposition is indicated by contemporaneous magmatic activity, oil generation and seeping and spilling of hydrocarbons. Earlier researchers have already noted that some C_{org}-rich Zaonega rocks have high-silica content possibly related to wide-scale hydrothermal circulation and silica-leaching during hydrocarbon formation and migration (Lepland et al., 2014; van Zuilen et al., 2012), which also points to silica association with hydrothermal fluids. Magmatically triggered intense hydrothermal fluid circulation within Zaonega rocks might have supplied water, silica, CO_2 and CH_4 to the depositional system (Črne et al., 2014; Črne et al., 2012a, b) and hydrothermal

fluids rich in CO_2 may have attacked dolomite and dissolved it while later precipitating their calcium content as calcite or calcite separates as solid-phases (Faust, 1949).

Silica precipitation from high temperature hydrothermal waters saturated in respect to silica occurs upon cooling, or the silica precipitation can be initiated by changing (lowering) pH conditions, both of which can be in place during silica supersaturated fluid circulation in the carbonate sediments (Raymond, 2002). Alternatively, it is also possible that during diagenesis, ion-migration of silica may result in its concentration in some beds and depletion in others. However, this is more common to dissolution and redistribution of biogenic amorphous silica in Phanerozoic sediments (Maliva et al., 1989; Raymond, 2002).

Our observations also show that large secondary calcite crystals occur specifically in the transition zones between chert and dolostone in Zaonega rocks suggesting fluidal replacement of dolomite and precipitation of secondary calcite, rather than silica redistribution. In addition, otherwise homogenous dolomite crystals in this zone show in scanning electron microscopy BSE images brighter patches indicating some dedolomitization and calcite precipitation within dolomite rhombohedra. In some cases dolomite is overgrown by calcite, which co-occurs with secondary quartz and apatite, indicating its relatively later formation in respect to dolomite. It is also important that central parts of the dolomite concretions and dolostone beds are composed of texturally similar tightly intergrown dolomite crystal aggregates. Tight crystal framework probably prevented intensive infiltration of later fluids, thus dolomite crystals in the central parts of the concretions and dolostone beds are less altered and unaffected by hydrothermal fluids. Therefore we suggest that carbonate concretions in the Shunga and Tetugino chert beds are relicts of the host rock, not concretions in the genetic sense.

Timing of the silicification of the Zaonega dolostones is somewhat difficult to assess. However, preservation of microfossils has been interpreted as an evidence for early timing of chertification (Knoll, 1985) and suspicious finds of possible microbial structures within chertified beds, if true at all, would suggest, thus, an early chertification. More importantly, textural data show no evidence for mechanical grain deformation nor pressure solution in silicified beds. Additionally, loose arrangement and well defined shapes of dolomite crystal ghosts in Zaonega chert suggest that silicification predated the carbonate mud compaction and (early) diagenetic recrystallization, and could be therefore considered very early diagenetic or even synsedimentary.

Conclusions

The chert beds found in the upper Zaonega Formation near Shunga and Tetugino villages have similar microtextures to Phanerozoic silicified carbonates, Petrographic observations of the chert beds, associated carbonate beds and concretions within chert beds, combined with geochemical data display associations of textures and minerals, such as quartz pseudomorphs after dolomite, dolomite crystal moulds and relict isolated dolomite inclusions in otherwise chemically uniform chert, dedolomitization and dolomite overgrowth by secondary calcite. These observations indicate that these cherts formed by carbonate replacement and therefore we suggest that the carbonate concretions in the Shunga and Tetugino chert beds are relicts of a carbonate host rock.

The sedimentary rocks of the Zaonega Formation were deposited in a magmatically active basin, in which intense hydrothermal fluid circulation might have supplied water, silica and CO_2 to the depositional system (Lepland et al., 2014; van Zuilen et al., 2012), suggesting that the silicification of the dolostone sediments of the Shunga and Tetugino outcrops was driven by hydrothermal fluids supersaturated in respect to silica. The timing of chertification is uncertain, but textural data showing no evidence for mechanical grain deformation nor pressure solution of dolomite pseudomorph aggregates in silicified beds suggest very early silification predating the compaction.

Acknowledgments

I would like to thank Lauri Joosu for his help and patience to answer all the questions raised by the course of this work. I also appreciate all the guidance and ideas by Aivo Lepland concerning the chertification of the Zaonega Formation rocks.

References

Bailey, J. V., Corsetti, F. A., Greene, S. E., Crosby, C. H., Liu, P., and Orphan, V. J., 2013, Filamentous sulfur bacteria preserved in modern and ancient phosphatic sediments: implications for the role of oxygen and bacteria in phosphogenesis: Geobiology, v. 11, no. 5, p. 397-405.

Buick, R., 1990, Microfossil recognition in Archean rocks; an appraisal of spheroids and filaments from a 3500 m.y. old chert-barite unit at North Pole, Western Australia: Palaios, v. 5, p. 441-459.

Chakrabarti, R., Knoll, A. H., Jacobsen, S. B., and Fischer, W. W., 2012, Si isotope variability in Proterozoic cherts: Geochimica Et Cosmochimica Acta, v. 91, p. 187-201.

Črne, A. E., Melezhik, V. A., Lepland, A., Fallick, A. E., Prave, A. R., and Brasier, A. T., 2014, Petrography and geochemistry of carbonate rocks of the Paleoproterozoic Zaonega Formation, Russia: Documentation of C-13-depleted non-primary calcite: Precambrian Research, v. 240, p. 79-93.

Črne, A. E., Melezhik, V. A., Prave, A. R., Lepland, A., Romashkin, A. E., Rychanchik, D. V., Hanski, E. J., and Luo, Z., 2012a, Zaonega Formation: FAR-DEEP Hole 13A, in Melezhik, V. A., Prave, A. R., Fallick, A. E., Hanski, E. J., Lepland, A., Kump, L. R., and Strauss, H., eds., Reading the Archive of Earth's Oxygenation: The Core Archive of the Fennoscandian Arctic Russia - Drilling Early Earth Project, Volume 2, Springer, p. 1008-1046.

-, 2012b, Zaonega Formation: FAR-DEEP Holes 12A and 12B, and Neighbouring quarries, in Melezhik, V. A., Prave, A. R., Fallick, A. E., Hanski, E. J., Lepland, A., Kump, L. R., and Strauss, H., eds., Reading the Archive of Earth's Oxygenation: The Core Archive of the Fennoscandian Arctic Russia - Drilling Early Earth Project, Volume 2, Springer, p. 946-1007.

Faust, G. T., 1949, Dedolomitization, and its relation to a possible derivation of a magnesium rich hydrothermal solution: U. S. Geological Survey, v. 34, p. 789-823.

Goldhammer, T., Bruchert, V., Ferdelman, T. G., and Zabel, M., 2010, Microbial sequestration of phosphorus in anoxic upwelling sediments: Nature Geoscience, v. 3, no. 8, p. 557-561.

Griffin, B. J., 2000, Charge contrast imaging of material growth and defects in environmental scanning electron miscroscopy - Linking electron emission and cathodoluminescence: Scanning, v. 22, no. 4, p. 234-242.

Hofmann, H. J., 1987, Paleoscene .7. Precambrian Biostratigraphy: Geoscience Canada, v. 14, no. 3, p. 135-154.

Joosu, L., Lepland, A., Kirsimäe, K., Romashkin, A. E., Roberts, N. M. W., Martin, A. P., and Črne, A., (submitted), Rare earth element composition of sedimentary apatite in 2.0 Ga Zaonega organic rich sediments: environmental setting of the phosphogenesis: Manuscript, Chemical Geology.

Karhu, J. A., and Holland, H. D., 1996, Carbon isotopes and the rise of atmospheric oxygen: Geology, v. 24, no. 10, p. 867-870.

Kastner, M., Keene, J. B., and Gieskes, J. M., 1977, Diagenesis of siliceous oozes—I. Chemical controls on the rate of opal-A to opal-CT transformation—an experimental study: Geochimica et Cosmochimica Acta, v. 41, no. 8, p. 1041–1051.

Knoll, A. H., 1985, The Distribution and Evolution of Microbial Life in the Late Proterozoic ERA: Annual Review of Microbiology, v. 39 p. 391-417.

Lepland, A., Joosu, L., Kirsimae, K., Prave, A. R., Romashkin, A. E., Crne, A. E., Martin, A. P., Fallick, A. E., Somelar, P., Upraus, K., Mand, K., Roberts, N. M. W., van Zuilen, M. A., Wirth, R., and Schreiber, A., 2014, Potential influence of sulphur bacteria on Palaeoproterozoic phosphogenesis: Nature Geoscience, v. 7, no. 1, p. 20-24.

Maliva, R. G., 2001, Silicification in the Belt Supergroup (Mesoproterozoic), Glacier National Park, Montana, USA: Sedimentology, v. 48, no. 4, p. 887-896.

Maliva, R. G., Knoll, A. H., and Siever, R., 1989, Secular Change in Chert Distribution: A Reflection of Evolving Biological Participation in the Silica Cycle: Palaios, v. 4, p. 519-532.

Maliva, R. G., Knoll, A. H., and Simonson, B. M., 2005, Secular change in the Precambrian silica cycle: Insights from chert petrology: Geological Society of America Bulletin, v. 117, no. 7-8, p. 835-845.

Melezhik, V. A., Fallick, A. E., Filippov, M. M., and Larsen, O., 1999a, Karelian shungite - an indication of 2.0-Ga-old metamorphosed oil-shale and generation of petroleum: geology, lithology and geochemistry: Earth-Science Reviews, v. 47, no. 1-2, p. 1-40.

Melezhik, V. A., Fallick, A. E., Medvedev, P. V., and Makarikhin, V. V., 1999b, Extreme C-13(carb) enrichment in ca, 2.0 Ga magnesite-stromatolite-dolomite- 'red beds' association in a global context: a case for the world-wide signal enhanced by a local environment: Earth-Science Reviews, v. 48, no. 1-2, p. 71-120.

Melezhik, V. A., Filippov, M. M., and Romashkin, A. E., 2004, A giant Palaeoproterozoic deposit of shungite in NW Russia: genesis and practical applications: Ore Geology Reviews, v. 24, no. 1-2, p. 135-154.

Melezhik, V. A., Medvedev, P. V., and Svetov, S. A., 2012, The Onega Basin, in Melezhik, V. A., Prave, A. R., Hanski, E. J., Fallick, A. E., Lepland, A., Kump, L. R., and Strauss, H., eds., Reading the Archive of Earth's Oxygenation: The Paleoproterozoic of Fennoscandia as Context for the Fennoscandian Arctic Russia - Drilling Early Earth Project., Volume 1, Springer, p. 249-287.

Ojakangas, R. W., Marmo, J. S., and Heiskanen, K. I., 2001, Basin evolution of the Paleoproterozoic Karelian Supergroup of the Fennoscandian (Baltic) Shield: Sedimentary Geology, v. 141, p. 255-285.

Ovchinnikova, G. V., Kuznetsov, A. B., Melezhik, V. A., Gorokhov, I. M., Vasil'eva, I. M., and Gorokhovskii, B. M., 2007, Pb-pb age of jatulian carbonate rocks: The tulomozero formation of Southeast Karelia: Stratigraphy and Geological Correlation, v. 15, no. 4, p. 359-372.

Perry, E. C., Lefticariu, L., and Lefticariu, J., 2005, Formation and Geochemistry of Precambrian Cherts, in Mackenzie, F. T., ed., Sediments, Diagenesis, and Sedimentary Rocks, Volume 7, Elsevier, p. 99-115.

Pirajno, F., and Grey, K., 2002, Chert in the Palaeoproterozoic Bartle Member, Killara Formation, Yerrida Basin, Western Australia: a rift-related playa lake and thermal spring environment (vol 113, pg 169, 2002): Precambrian Research, v. 116, no. 3-4, p. 355-355.

Posth, N. R., Hegler, F., Konhauser, K. O., and Kappler, A., 2008, Alternating Si and Fe deposition caused by temperature fluctuations in Precambrian oceans: Nature Geoscience, v. 1, no. 10, p. 703-708.

Puchtel, I. S., Brugmann, G. E., and Hofmann, A. W., 1999, Precise Re-Os mineral isochron and Pb-Nd-Os isotope systematics of a mafic-ultramafic sill in the 2.0 Ga Onega plateau (Baltic Shield): Earth and Planetary Science Letters, v. 170, no. 4, p. 447-461.

Ramseyer, K., Amthor, J. E., Matter, A., Pettke, T., Wille, M., and Fallick, A. E., 2013, Primary silica precipitate at the Precambrian/Cambrian boundary in the South Oman Salt Basin, Sultanate of Oman: Marine and Petroleum Geology, v. 39, no. 1, p. 187-197.

Raymond, L. A., 2002, Cherts, Evaporites, and Other Precipitated Rocks, in Kemp, M. J., and Russian, R., eds., Petrology: The Study of Igneous, Sedimentary and Metamorphic Rocks, McGraw-Hill p. 436-447.

Robertson, K., Gauvin, R., and Finch, J., 2005, Application of charge contrast imaging in mineral characterization: Minerals Engineering, v. 18, no. 3, p. 343-352.

Schulz, H. N., and Schulz, H. D., 2005, Large sulfur bacteria and the formation of phosphorite: Science, v. 307, no. 5708, p. 416-418.

Siever, R., 1992, The Silica Cycle in the Precambrian: Geochimica Et Cosmochimica Acta, v. 56, no. 8, p. 3265-3272.

Strauss, H., Melezhik, V. A., Lepland, A., Fallick, A. E., Hanski, E. J., Filippov, M. M., Deines, Y. E., Illing, J. C., Crne, A. E., and Brasier, A. T., 2012, Enhanced Accumulation of Organic Matter: The Shunga Event, in Melezhik, V. A., Kump, L. R., Fallick, A. E., Strauss, H., Hanski, E. J., Prave, A. R., and Lepland, A., eds., Reading the Archive of Earth's Oxygenation: Global Events and the Fennoscandian Artic Russia - Drilling Early Earth Project, Volume 3, Springer, p. 1195-1273.

van Zuilen, M. A., Fliegel, D., Wirth, R., Lepland, A., Qu, Y. G., Schreiber, A., Romashkin, A. E., and Philippot, P., 2012, Mineral-templated growth of natural graphite films: Geochimica Et Cosmochimica Acta, v. 83, p. 252-262.

Watt, G. R., Griffin, B. J., and Kinny, P. D., 2000, Charge contrast imaging of geological materials in the environmental scanning electron microscope: American Mineralogist, v. 85, no. 11-12, p. 1784-1794.

Zaonega kihistu dolokivide ränistumine

Kärt Üpraus

Kokkuvõte

Paleoproterosoilise Onega basseini (Karjala) Zaonega kihistu läbilõike ülemise osa moodustab orgaanilise ainese rikka mudakivi, dolokivimite ja ränikivimite vaheldumine, mida lõikavad arvukad settimisega samaaegselt sissetunginud aluselised magmakivimite sillid ja laavad.

Ränikivimid, nagu Zaonega kihistu läbilõigetes, võivad tekkelt olla settelised või asenduslikud. Settelised ränikivimid nagu tänapäevastes ookeanides moodustuvad valdavalt ookeanide pinnakihis elvate amorfsest räniainesest (opaalA) toesega organismide (radiolaarid, ränivetikad) jäänuste kuhjumisel ja ümberkristalliseerumisel. Settelised ränikivimid võivad moodustuda ka lahustunud räniainese piisaval üleküllastusel otsese väljasettimisena nagu seda on arvatud osade Arhaikumi ja Proterosoikumi kihiliste ränikivimite puhul. Asenduslik ränistumine on tüüpiline karbonaatkivimitele, kus sissetungivate diageneetiliste või hüdrotermaalsete lahuste toimel kaltsiit/dolomiit asendataks mikrokristallilise kvartsiga. Asenduslik ränistumine on tuntud nii Fanerosoikumi kui ka Eelkambriumi setendites.

Käesoleva uurimuse eesmärgiks oli selgitada Zaonega kihistu ränikivimite setteline või asenduslik päritolu. Uuritud materjal pärineb Zaonega kihistu ülemist osa avavatest paljanditest Shunga ja Titjugino külade lähistel Karjalas. Uuritud ränikivimite ja nendega seotud karbonaatide ning karbonaatsete konkretsioonide petrograafilised, mineraloogilised ja geokeemilised analüüsid näitavad mitmekesiseid struktuure ja mineraalide kooslusi nagu kvartsi pseudomorfoose dolomiidi järgi ja reliktseid isoleeritud dolomiidi suletisi muidu keemiliselt/mineraalselt ühetaolises ränikivimis, dedolomitiseerumis nähtusi ja sekundaarse kaltsiidi ülekasveid dolomiidi kristallidel, samuti ühtlaselt mikrokristallilist kvartsi (<5 μm) kõigis uuritud ränikivimites. Need tulemused näitavad, et uuritud ränikivimid on olemuslikult asenduslikud ning moodustusid algse dolokivimi (karbonaatse muda) ränistumisel kas diageneetiliste ja/või hüdrotermalsete fluidide toimel.

Zaonega kihistu settekivimid moodustusid magmaliselt aktiivses basseinis, kus intensiivne hüdrotermaalne tsirkulatsioon võis settesüsteemi varustada vee, räni ja CO_2-ga (Lepland et al., 2014; van Zuilen et al., 2012). Eelnevast lähtudes võib arvata, et Shunga ja Titjugino dolomiitsete setete ränistumine oli tingitud räni suhtes üleküllastunud hüdrotermaalsete

fluidide reageerimisel karbonaatkivimitega. Ränistumise vanus on ebaselge, kuid ränikivimi kihtides esinevad võimalikud mikroobsed struktuurid, mis viitavad ränistumise varadiageneetilisele olemusele (Maliva et al., 1989; Maliva et al., 2005). Seda järeldust toetab ka asendunud dolomiidi väliskujude hea säilivus ja poorne struktuur, mis ei näita mehaanilist tihenemist ega rõhulist üleslahustumist (stüloliidistumist), mis viitab ränistumisele enne sette ümberkriatalliseerumist ja olulist tihenemist.

Non-exclusive licence to reproduce thesis and make thesis public

I, Kärt Üpraus,

1. herewith grant the University of Tartu a free permit (non-exclusive licence) to:

1.1. reproduce, for the purpose of preservation and making available to the public, including for addition to the DSpace digital archives until expiry of the term of validity of the copyright, and

1.2.make available to the public via the web environment of the University of Tartu, including via the DSpace digital archives until expiry of the term of validity of the copyright,

Chert-dolostone sequences in Zaonega Formation, Karelia: implication to the chert origin,

supervised by Kalle Kirsimäe,

2. I am aware of the fact that the author retains these rights.

3. I certify that granting the non-exclusive licence does not infringe the intellectual property rights or rights arising from the Personal Data Protection Act.

Tartu, **23.05.2014**